



HAL
open science

Noise predictions of a Mach 0.9 round jet using tailored adjoint Green's functions

Etienne Spieser, Christophe Bogey, Christophe Bailly

► **To cite this version:**

Etienne Spieser, Christophe Bogey, Christophe Bailly. Noise predictions of a Mach 0.9 round jet using tailored adjoint Green's functions. *Journal of Sound and Vibration*, 2023, 10.1016/j.jsv.2022.117532 . hal-03932694

HAL Id: hal-03932694

<https://hal.science/hal-03932694>

Submitted on 10 Jan 2023

HAL is a multi-disciplinary open access archive for the deposit and dissemination of scientific research documents, whether they are published or not. The documents may come from teaching and research institutions in France or abroad, or from public or private research centers.

L'archive ouverte pluridisciplinaire **HAL**, est destinée au dépôt et à la diffusion de documents scientifiques de niveau recherche, publiés ou non, émanant des établissements d'enseignement et de recherche français ou étrangers, des laboratoires publics ou privés.

Journal Pre-proof

Noise predictions of a Mach 0.9 round jet using tailored adjoint Green's functions

Étienne Spieser, Christophe Bogey, Christophe Bailly



PII: S0022-460X(22)00715-5
DOI: <https://doi.org/10.1016/j.jsv.2022.117532>
Reference: YJSVI 117532

To appear in: *Journal of Sound and Vibration*

Received date : 14 February 2022
Revised date : 19 December 2022
Accepted date : 19 December 2022

Please cite this article as: É. Spieser, C. Bogey and C. Bailly, Noise predictions of a Mach 0.9 round jet using tailored adjoint Green's functions, *Journal of Sound and Vibration* (2022), doi: <https://doi.org/10.1016/j.jsv.2022.117532>.

This is a PDF file of an article that has undergone enhancements after acceptance, such as the addition of a cover page and metadata, and formatting for readability, but it is not yet the definitive version of record. This version will undergo additional copyediting, typesetting and review before it is published in its final form, but we are providing this version to give early visibility of the article. Please note that, during the production process, errors may be discovered which could affect the content, and all legal disclaimers that apply to the journal pertain.

© 2022 Published by Elsevier Ltd.

Noise predictions of a Mach 0.9 round jet using tailored adjoint Green's functions

Étienne Spieser*, Christophe Bogey, Christophe Bailly

Laboratoire de Mécanique des Fluides et d'Acoustique, Université de Lyon, CNRS, École Centrale de Lyon, Institut National des Sciences Appliquées de Lyon, Université Claude Bernard Lyon I, UMR 5509, 69130 Écully, France

Abstract

The turbulent mixing noise radiated by a Mach 0.9 jet is investigated. The focus is put on the proper calculation of acoustic propagation effects by means of adjoint Green's function that are tailored to the jet mean flow. Tam and Auriault's statistical mixing noise model is recast for Pierce's wave equation that is energy preserving. An unconditionally stable formulation to compute propagation effects is thus obtained. Adjoint fields are computed from the direct problem with help of the flow reversal theorem. A finite element solver is used to solve tailored adjoint Green's functions, and corresponding adjoint fields are displayed. Acoustic predictions are carried out for a wide range of polar angles, and compared to measurements. A particular attention is given to predictions achieved at upstream observer angles. At these angles, the present model describes the physics of upstream travelling guided jet waves. The adjoint method provides a suitable framework to split the generation of sound from its propagation. It is illustrated how tailored adjoint Green's functions filter the radiating part of Tam and Auriault's sound source model, by weighting with propagation effects.

Keywords: jet noise, sound propagation, adjoint method, tones.

*Corresponding author

Email address: etienne.spieser@ec-lyon.fr (Étienne Spieser)

1. Introduction

The modelling of turbulent mixing noise involves the expression of the noise spectrum S_{pp} . This quantity is of interest in many applications dealing with subsonic jet noise, including acoustic certification of aircraft [26]. For a microphone located at \mathbf{x}_m , the spectrum is obtained by considering the Fourier transform of the pressure autocorrelation defined in [Appendix A](#),

$$S_{pp}(\mathbf{x}_m, \omega) = \int_{\mathbb{R}} d\tau \overline{p(\mathbf{x}_m, \bullet)p(\mathbf{x}_m, \bullet + \tau)} e^{i\omega\tau} \quad (1)$$

where ω denotes the angular frequency, **where \bullet stands for a dummy time variable**, and where a stationary noise generation mechanism is assumed. Let us introduce Green's function $G_{\mathbf{x}_s, t_s}^{(\mathbf{x}_m, t_m)}$ to realise sound propagation from the source region Ω to the microphone one,

$$p(\mathbf{x}_m, t_m) = \int_{\mathbb{R}} dt_s \int_{\Omega} d\mathbf{x}_s G_{\mathbf{x}_s, t_s}^{(\mathbf{x}_m, t_m)} q(\mathbf{x}_s, t_s) \quad (2)$$

where (\mathbf{x}_m, t_m) and (\mathbf{x}_s, t_s) are associated with the observer and a current source in Ω respectively, q is the source term. The propagation problem is moreover time-shift invariant, $G_{\mathbf{x}_s, t_s}^{(\mathbf{x}_m, t_m)} = G_{\mathbf{x}_s}^{(\mathbf{x}_m, t_m - t_s)}$ for a steady base flow.

Acoustic analogies are often used in this context to reduce the computational cost, Lighthill's acoustic analogy [44] being the first and most famous formulation. In these approaches where the sound propagation is explicitly separated from generation, the spectrum S_{pp} is expressed from the two-point correlation R_{qq} of the source term,

$$S_{pp}(\mathbf{x}_m, \omega) = \int_{\mathbb{R}} d\tau \int_{\mathbb{R}} dt_1 \int_{\mathbb{R}} dt_2 \int_{\Omega} d\mathbf{x}_1 \int_{\Omega} d\mathbf{x}_2 G_{\mathbf{x}_1}^{(\mathbf{x}_m, t_1)} G_{\mathbf{x}_2}^{(\mathbf{x}_m, t_2 + \tau)} R_{qq}(\mathbf{x}_1, \mathbf{x}_2, t_1 - t_2) e^{i\omega\tau} \quad (3)$$

5 In the past, most of the efforts of improvements have focused in finding a proper description of the source correlation term R_{qq} by modelling the sound stemming from fluid dilatation [52, 63], from the quadrupole correlations arising in isotropic turbulence [53, 11, 40] or those from more complex shell models of turbulence [33, 4, 5]. The definition of the source term q and its associated wave
10 equation is also a critical step [45, 46, 29]. These modellings are however not so

often used in practice because the numerical determination of Green's function $G_{\mathbf{x}_1}$ and $G_{\mathbf{x}_2}$ for all positions $\mathbf{x}_1, \mathbf{x}_2$ in the source domain Ω is not affordable.

Lagrange's identity [41, 59] provides an especially suitable framework to shape further statistical models in giving a better account of sound propagation. By using the reciprocity principle in its most general form that involves adjoints, Green's functions for the acoustic propagation can be recast to depend solely on the receiver [25, 59],

$$G_{\mathbf{x}_s, t_s}^{(\mathbf{x}_m, t_m)} = G_{\mathbf{x}_m, t_m}^\dagger(\mathbf{x}_s, t_s) \quad (4)$$

where $G_{\mathbf{x}_m, t_m}^\dagger$ is adjoint Green's function expressed for the microphone position \mathbf{x}_m and time t_m , and for which a tacit choice of a suitable scalar product is made.

The first reformulation of Lighthill's acoustic analogy in the adjoint framework was proposed by Dowling *et al.* [25]. A major contribution was made by Tam and Auriault [62, 63] for statistical jet noise modelling. Goldstein and Leib [31, 42, 32], Raizada and Morris [51] amongst other, proposed additional statistical jet noise models involving adjoints later on.

Statistical jet noise modelling has benefitted from the advances in computational science in providing an access to an accurate description of the source term's correlation R_{qq} [12, 24, 43] and in informing on the manner flow structures radiate to the observer [18, 67, 1]. Solving numerically adjoint Green's functions for arbitrary base flows and geometries has remained a challenge, and beside contributions done in the group of Karabasov [38, 58], only adjoint Green's function tailored to some specific flow profiles have been used to account for the sound propagation in statistical models. In that case, adjoint Green's functions are often not known analytically, but their governing equations are smartly rearranged so to be tractable by ordinary differential equations. Sound is then considered to propagate either in the free field [47, 30], over a plug flow [25], over a general parallel jet flow [62, 51, 2] or over a slowly diverging jet flow [31, 34, 7, 8, 6].

Spieser and Bailly [59] recently proposed the use of Pierce's wave equation to

35 compute sound propagation in the adjoint framework. The self-adjoint nature
of this operator possesses two main advantages, it guaranties the stability of the
sound propagation problem and enables the computation of the adjoints with
help of the handy flow reversal theorem. This study intends to evaluate numer-
ically such adjoint Green's functions using a finite element solver, and aims to
40 illustrate how the modelling and the understanding of jet noise can thereby be
improved. Tam *et al.* [65, 66] already highlighted on an experimental campaign
how the adjoint formalism could be used to characterise and extrapolate the
radiating parts of the coherent structures in jets. As explained in their study,
the whole sound source is not contributing to the acoustic radiation, in fact,
45 only the part filtered by the wave operator is. Green's functions are the formal
inverse of an operator and adjoint Green's functions are therefore the appro-
priate tool to isolate the radiating parts of a sound source. On the basis of
this observation, this contribution also means to illustrate how insight into the
radiating parts of a jet can be gained within the adjoint framework.

50 The paper is organised as follows. Tam and Auriault's mixing noise model is
reformulated for Pierce's wave equation in section § 2. The numerical procedure
to compute tailored adjoint Green's functions in an efficient way is explained in
section § 3. Mixing noise radiated in the sideline direction by a subsonic round
jet at Mach 0.9 is investigated in section § 4. Section § 5 is focused on the
55 acoustic field radiated in the upstream direction and the emergence of tones.
The influence of the nozzle for the computation of the acoustic field is discussed,
and predictions for a wide range of polar angles are presented in section § 6.
Concluding remarks are finally drawn in the last section. Calculation details
have been included in the appendices for ease of reading.

60 **2. Jet mixing noise model for Pierce's wave equation**

Tam *et al.* [64] gave experimental evidences for two contributions arising in
the turbulent mixing noise process of a jet. The first one is associated with the
large-scales of turbulence, often associated with the development of convective

instability waves, while the second one originates from the turbulence fine scale.
 65 Shortly after, Tam and Auriault [63] proposed a statistical model to predict the
 noise spectra radiated by the **latter** component. The concern of this section
 is to reformulate their model for Pierce's wave equation.

2.1. Prequel of Tam and Auriault's model

The starting point for this model is based on an acoustic analogy, where the
 sound generation process and its propagation over a base flow are addressed
 separately. A parallel and steady base flow is assumed and forced linearised
 Euler's equation reads as,

$$\begin{cases} \rho_0 \frac{D(\mathbf{u})}{Dt} + \nabla p = -\nabla \cdot (\rho_0 \mathbf{u} \otimes \mathbf{u}) \\ \frac{D(p)}{Dt} + \gamma p_0 (\nabla \cdot \mathbf{u}) = 0 \end{cases} \quad (5)$$

where $D/Dt = \partial/\partial t + \mathbf{u}_0 \cdot \nabla$ is the material derivative along the mean flow.
 The fluctuating variables are written without subscript nor superscript, and the
 mean flow field **is** indexed with $_0$. The non linear source term on the right-hand
 side of the momentum equation has been identified by Bogey *et al.* [19] and
 discussed later [9]. As also underlined in these previous studies, Pierce's wave
 equation does not describe instability waves [59] and is therefore particularly
 well suited to be used in an acoustic analogy. Introducing the acoustic potential
 ϕ as $p = -D(\phi)/Dt$, and a_0 the speed of sound, an acoustic analogy based on
 Pierce's equation can be derived [49, 59],

$$\frac{D^2(\phi)}{Dt^2} - \nabla \cdot (a_0^2 \nabla \phi) = \frac{D(S_m)}{Dt}, \quad \nabla^2 S_m = \nabla \cdot \nabla \cdot (\rho_0 \mathbf{u} \otimes \mathbf{u}) \quad (6)$$

where the source term presented in equation (6) has been reduced to its main
 contribution provided by Reynolds stress tensor. A drastic simplification of the
 source term is considered in Tam and Auriault [63] by contracting the instan-
 taneous Reynolds stress tensor $\rho_0 \mathbf{u} \otimes \mathbf{u} \approx q_s \mathbf{I}$, where q_s is linked to the
 turbulent kinetic energy and \mathbf{I} is the identity matrix. As a result, the source
 term in equation (5) is reduced to,

$$-\nabla \cdot (\rho_0 \mathbf{u} \otimes \mathbf{u}) \approx -\nabla q_s \quad (7)$$

and its quadrupolar feature is lost. Identification with the acoustic analogy built for Pierce's wave equation (6) is straightforward and leads to,

$$S_m = -q_s \quad (8)$$

2.2. Recast of the model

70 2.2.1. Adjoint statement of the problem

Pierce's wave equation (6) is self-adjoint for the canonical scalar product defined in [Appendix A](#), and its adjoint Green's function $\phi_{\mathbf{x}_m, t_m}^\dagger$ is the anti-causal solution of,

$$\frac{D^2(\phi_{\mathbf{x}_m, t_m}^\dagger)}{Dt^2} - \nabla \cdot (a_0^2 \nabla \phi_{\mathbf{x}_m, t_m}^\dagger) = \delta_{\mathbf{x}_m, t_m} \quad (9)$$

where $\delta_{\mathbf{x}_m, t_m}$ is the Dirac delta function taken at the microphone position \mathbf{x}_m and time t_m . Applying Lagrange's identity [59, eq. (4.4)] with adjoint Green's function $\phi_{\mathbf{x}_m, t_m}^\dagger$ then directly leads to,

$$\phi(\mathbf{x}_m, t_m) = \langle \phi_{\mathbf{x}_m, t_m}^\dagger, -\frac{D(q_s)}{Dt} \rangle \quad (10)$$

2.2.2. Calculation of the acoustic noise spectra

Choosing Pierce's wave equation to describe the propagation of sound, the acoustic spectral density S_{pp} , equation (1), can then be recast as,

$$S_{pp}(\mathbf{x}_m, \omega) = \int_{\mathbb{R}} d\tau \frac{D(\phi)}{D_{\bullet, \mathbf{x}_m}} \overline{\frac{D(\phi)}{D_{\bullet, \mathbf{x}_m + \tau}} e^{i\omega\tau}} \quad (11)$$

where $D/D_{t_A, \mathbf{x}_B} = \partial/\partial t_A + \mathbf{u}_0 \cdot \partial/\partial \mathbf{x}_B$ is the material derivative with respect to the position \mathbf{x}_B and the reference time t_A . This cumbersome notation is used in the following whenever there may be a confusion in the variables on which the material derivative applies and is omitted elsewhere. Following the derivations provided in [Appendix B](#), expressing previous relationship with help of adjoint Green's functions, leads to,

$$S_{pp}(\mathbf{x}_m, \omega) = \int_{\mathbb{R}} d\tau \int_{\Omega} d\mathbf{x}_1 \int_{\Omega} d\mathbf{x}_2 \int_{\mathbb{R}} d\tilde{t}_1 \int_{\mathbb{R}} d\tilde{t}_2 \frac{D(\phi_{\mathbf{x}_m}^\dagger(\mathbf{x}_1, \tilde{t}_1))}{D_{-\tilde{t}_1, \mathbf{x}_m}} \frac{D(\phi_{\mathbf{x}_m}^\dagger(\mathbf{x}_2, \tilde{t}_2 - \tau))}{D_{-\tilde{t}_2, \mathbf{x}_m}} R_{QQ}(\mathbf{x}_1, \mathbf{x}_2, \tilde{\tau}) e^{i\omega\tau} \quad (12)$$

where $\tilde{\tau} = \tilde{t}_1 - \tilde{t}_2$ is the time separation and R_{QQ} is the space-time correlation defined as,

$$R_{QQ}(\mathbf{x}_1, \mathbf{x}_2, \tilde{\tau}) \equiv \frac{\overline{D(q_s(\mathbf{x}_1, \bullet + \tilde{\tau})) D(q_s(\mathbf{x}_2, \bullet))}}{D_{\bullet, \mathbf{x}_1} D_{\bullet, \mathbf{x}_2}} \quad (13)$$

To compute the acoustic spectral density, only the time-shifts in the source correlation are of significance. Adjoint Green's functions and the material derivative that apply on them can thus be expressed in the frequency domain to obtain the concise form,

$$S_{pp}(\mathbf{x}_m, \omega) = \int_{\Omega} d\mathbf{x}_1 \int_{\Omega} d\mathbf{x}_2 D_{-\mathbf{u}_0, \mathbf{x}_m} \left(\phi_{\mathbf{x}_m}^{\dagger}(\mathbf{x}_1, \omega) \right) D_{-\mathbf{u}_0, \mathbf{x}_m} \left(\phi_{\mathbf{x}_m}^{\dagger}(\mathbf{x}_2, -\omega) \right) \int_{\mathbb{R}} d\tilde{\tau} R_{QQ}(\mathbf{x}_1, \mathbf{x}_2, \tilde{\tau}) e^{-i\omega\tilde{\tau}} \quad (14)$$

where the Fourier transform conventions introduced in Appendix A are chosen. Equation (14) is the most advanced expression of the noise spectrum that can be derived from equations (6) and (7) without introducing further hypothesis.

75 2.2.3. Far field approximation

In classical jet noise applications, Fraunhofer's far field condition is satisfied [36]. This approximation is made here to make the evaluation of the double volume integral over the source region more tractable. Introducing the separation vector $\mathbf{r} = \mathbf{x}_1 - \mathbf{x}_2$ between two points \mathbf{x}_1 and \mathbf{x}_2 in the jet region, enables to link an acoustic ray reaching an observer position \mathbf{x}_m to a neighbouring ray by modelling only the phase shift in between them. Following Tam and Auriault's work, two neighbouring acoustic ray paths are related by,

$$\phi_{\mathbf{x}_m}^{\dagger}(\mathbf{r} + \mathbf{x}_2, \omega) \approx \phi_{\mathbf{x}_m}^{\dagger}(\mathbf{x}_2, \omega) \exp\left(\frac{i\omega \mathbf{x}_m \cdot \mathbf{r}}{a_{\infty} |\mathbf{x}_m|}\right) \quad (15)$$

where a_{∞} is the ambient speed of sound. Replacing this formula in the expression of S_{pp} , and some calculus detailed again in Appendix B provide,

$$S_{pp}(\mathbf{x}_m, \omega) = \int_{\Omega} d\mathbf{x}_s \left| D_{-\mathbf{u}_0, \mathbf{x}_m} \left(\phi_{\mathbf{x}_m}^{\dagger}(\mathbf{x}_s, \omega) \right) \right|^2 \int_{\Omega} d\mathbf{r} \int_{\mathbb{R}} d\tilde{\tau} R_{QQ}(\mathbf{x}_s, \mathbf{r}, \tilde{\tau}) e^{i\omega \left[\frac{\mathbf{x}_m \cdot \mathbf{r}}{a_{\infty} |\mathbf{x}_m|} - \tilde{\tau} \right]} \quad (16)$$

Please note that the use of this far-field approximation implies a simplification of the physics of the problem, as no phase differences are accounted for when

$\mathbf{x}_m \cdot \mathbf{r} = 0$, according to equation (15). Depending on the expression of the source correlation term R_{QQ} , this approximation may thus entail a singularity for observer located in a direction normal to the jet axis. In particular, if at the leading order in \mathbf{r} , the expression of the source correlation behaves in $R_{QQ} \propto \exp(|\mathbf{r}|^\alpha)$, then it becomes singular for an observer located normal to the jet axis when $\alpha \leq 1$. Future study may investigate the benefit of using a Taylor expansion to replace equation (15).

2.2.4. Modelling of the source correlation term R_{QQ}

In this study, the Q -quantity space-time correlation model used by Tam and Auriault [63, eq. (27)][52, § III.] is considered,

$$R_{QQ}(\mathbf{x}_s, \mathbf{r}, \tilde{\tau}) = \frac{\hat{q}_s^2}{\tau_s^2} \exp\left(-\frac{|\mathbf{r} \cdot \mathbf{u}_0|}{u_0^2 \tau_s} - \frac{\ln(2)}{l_s^2} (\mathbf{r} - \tilde{\tau} \mathbf{u}_0)^2\right) \quad (17)$$

where $u_0 = |\mathbf{u}_0|$. In other words, turbulence is assumed to be locally homogeneous. The mean velocity \mathbf{u}_0 and the local quantities \hat{q}_s , τ_s and l_s measuring the turbulence intensity, decay time and correlation length, are informed by the statistics of the flow as provided for instance by a Reynolds-averaged Navier-Stokes flow solution. These three variables are function of the position \mathbf{x}_s in the jet volume. This model for the source correlation R_{QQ} result in subsequent expression for the sound pressure level S_{pp} , details are provided in Appendix B,

$$S_{pp}(\mathbf{x}_m, \omega) = \int_{\Omega} d\mathbf{x}_s \frac{2\hat{q}_s^2 l_s^3}{\tau_s} \left(\frac{\pi}{\ln(2)}\right)^{3/2} \left| D_{-\mathbf{u}_0, \mathbf{x}_m} \left(\phi_{\mathbf{x}_m}^\dagger(\mathbf{x}_s, \omega) \right) \right|^2 \exp\left(\frac{-\omega^2 l_s^2}{4 \ln(2) u_0^2} \left(1 + \frac{u_0^2 |\mathbf{x}_{m,\perp}|^2}{a_\infty^2 |\mathbf{x}_m|^2}\right)\right) \frac{1}{1 + \omega^2 \tau_s^2 \left(1 - \frac{\mathbf{u}_0 \cdot \mathbf{x}_m}{a_\infty |\mathbf{x}_m|}\right)^2} \quad (18)$$

where $\mathbf{x}_{m,\perp} = \mathbf{x}_m - (\mathbf{x}_m \cdot \mathbf{u}_0) \mathbf{u}_0 / u_0^2$, and where $D_{-\mathbf{u}_0, \mathbf{x}_m}$ is the material derivative along $-\mathbf{u}_0$ taken at the position \mathbf{x}_m and expressed in the frequency domain. This relation is comparable with the one proposed by Tam and Auriault [63, eq. (35)], apart from original adjoint Green's function $p_{\mathbf{x}_m}^\dagger(\mathbf{x}_s, \omega)$ that is replaced by $D_{-\mathbf{u}_0, \mathbf{x}_m} \left(\phi_{\mathbf{x}_m}^\dagger(\mathbf{x}_s, \omega) \right)$.

2.2.5. Final expression

The material derivative $D_{-\mathbf{u}_0, \mathbf{x}_m} \left(\phi_{\mathbf{x}_m}^\dagger(\mathbf{x}_s, \omega) \right)$ can be expressed analytically in presence of flight effects, that is when the ambient media is moving at a constant velocity \mathbf{u}_f . The intermediate steps are reported in Appendix B. In the end, for a microphone located in the far-field at an angle θ_m from the jet axis, as illustrated in figure 3, Tam and Auriault's mixing noise formula can be recast for Pierce's wave equation into,

$$S_{pp}(\theta_m, \omega) = \int_{\Omega} d\mathbf{x}_s \frac{2\omega^2 \hat{q}_s^2 l_s^3}{\tau_s} \left(\frac{\pi}{\ln(2)} \right)^{3/2} \left| \phi_{\theta_m}^\dagger(\mathbf{x}_s, \omega) \right|^2 \left(1 + \frac{M_f \cos \theta_m}{1 + M_f \cos \theta_m} \right)^2 \frac{\exp \left(\frac{-\omega^2 l_s^2}{4 \ln(2) u_0^2} (1 + M_\infty^2 \sin^2 \theta_m) \right)}{1 + \omega^2 \tau_s^2 (1 - M_\infty \cos \theta_m)^2} \quad (19)$$

where $M_\infty = u_0/a_\infty$ is the local acoustic Mach number and the flight Mach number is $M_f = |\mathbf{u}_f|/a_\infty$. The azimuthal dependency on the microphone position ψ_m is not accounted for, it is however fairly straightforward to include such effects in the derivations.

2.3. Calibration of the parameters

In the present analysis, the parameters \hat{q}_s , τ_s and l_s appearing in equation (19) are informed by a statistical description of the jet flow. This is often performed from a Reynolds-averaged Navier-Stokes solution. Here, the statistical results considered for the modelling are obtained from the large-eddy simulation (LES) of an isothermal jet at a Mach number of 0.9 and a Reynolds number based on the diameter D_J of $Re_{D_J} = 10^5$. The LES has been carried out using an in-house solver of the three-dimensional filtered compressible Navier-Stokes equations in cylindrical coordinates based on low-dissipation and low-dispersion explicit schemes using a grid containing approximately one billion points [13]. The jet originate at $z = 0$ from a straight pipe nozzle of radius $D_J/2$ and length D_J , into a medium at rest at a temperature 293 K and a pressure 10^5 Pa. A Blasius laminar boundary-layer profile is imposed for the

axial velocity at the pipe inlet at $z = -D_J$, yielding a momentum boundary-
 110 layer thickness of $0.009D_J$ at the exit. Random low-level vortical disturbances
 are also added inside the pipe [21, 22] with a magnitude adjusted to obtain a
 peak turbulence intensity of 9% at the exit. During the simulation, density,
 velocity components and pressure have been recorded at several locations dur-
 ing a time of $T = 2000D_J/u_j$, creating a data base described in reference [16],
 115 for instance. More details and results of the jet LES can be found in previous
 studies [1, 14, 17].

In their contribution, Tam and Auriault proposed to model the parameters
 \hat{q}_s , τ_s and l_s from a k - ε flow solution [63] considering following relationships,

$$l_s \propto \frac{k^{3/2}}{\varepsilon}, \quad \tau_s \propto \frac{k}{\varepsilon} \quad \text{and,} \quad \hat{q}_s \propto \rho_0 k \quad (20)$$

so that only three constants were left to calibrate. In this work the number
 of independent variables is reduced to two by assuming that the characteristic
 time scale τ_s , which corresponds to the life time of turbulence, and length scale
 l_s of Tam and Auriault's model are related in a moving reference frame by u'_{ref}
 that is a measure of the turbulent velocity, such as,

$$\tau_s = \frac{l_s}{u'_{\text{ref}}}, \quad \text{with,} \quad u'_{\text{ref}} = \sqrt{\frac{2}{3}k_{\text{max}}} \quad (21)$$

and, where $k_{\text{max}} \equiv k_{\text{max}}(z)$ is the maximum value of the turbulent kinetic energy
 k in a plane of constant z . From dimensional considerations, k [$m^2.s^{-2}$] and ε
 [$m^2.s^{-3}$] must then be linked by a characteristic time scale of the mean flow [56]
 [10, chap.9]. In the following, the turbulent dissipation rate ε is reconstructed
 from,

$$\varepsilon \propto k \left| \frac{\partial u_z}{\partial r} \right|_{\text{max}} \quad (22)$$

where $|\partial u_z / \partial r|_{\text{max}} \equiv |\partial u_z / \partial r|_{\text{max}}(z)$ is the maximal shear in a plane of constant
 z . Finally from equations (20) and (22), l_s can be expressed as,

$$l_s \propto \sqrt{k} / \left| \frac{\partial u_z}{\partial r} \right|_{\text{max}} \quad (23)$$

Only the mean flow and turbulent kinetic energy k are consequently required
 to calibrate l_s and τ_s . This is expected to make the calibration procedure fairly
 independent from the flow solver.

It is now argued that l_s corresponds to an integral length scale of the turbulence computed in a direction transverse to the jet flow. Let us consider a given instant of the source such that $\tilde{\tau} = 0$, and let σ be the standard deviation associated to the Gaussian source correlation R_{QQ} , then $R_{QQ}(\mathbf{x}_s, \mathbf{r}, \tilde{\tau} = 0) = (\hat{q}_s^2/\tau_s^2) \exp(-\mathbf{r}^2/(2\sigma^2))$. From the expression of R_{QQ} presented in equation (17), the source correlation can be expressed as $R_{QQ}(\mathbf{x}_s, \mathbf{r}, \tilde{\tau} = 0) = (\hat{q}_s^2/\tau_s^2) \exp(-\ln(2)\mathbf{r}^2/l_s^2)$, whenever $\mathbf{r} \cdot \mathbf{u}_0 = 0$. Thus for a separation vector transverse to the flow direction, $l_s = \sqrt{2\ln(2)}\sigma$ which is precisely the expression of the half width at the half maximum of a Gaussian distribution. To verify that this measure is equal to an integral length scale l_i , this latter length is computed in the transverse direction from the source correlation function given in equation (17),

$$l_i(\mathbf{x}_s) = \int_0^\infty \frac{R_{QQ}(\mathbf{x}_s, (0, \xi, 0), 0)}{|R_{QQ}(\mathbf{x}_s, \mathbf{0}, 0)|} d\xi = \int_0^\infty e^{-\frac{\ln(2)\xi^2}{l_s(\mathbf{x}_s)^2}} d\xi = \frac{l_s(\mathbf{x}_s)}{2} \sqrt{\frac{\pi}{\ln(2)}} \approx 1.064 l_s(\mathbf{x}_s) \quad (24)$$

120 It turns out that l_s corresponds to the transversal integral length scale of the Gaussian distribution R_{QQ} within 6%.

Without any direct access to the distribution of R_{QQ} , the latter distribution is assumed to be similar to that of $R_{u'_z u'_z}$. There are experimental [28] and theoretical [53, 3] arguments indicating that turbulence in the plumes of jets can reasonably be assumed as homogeneous and isotropic. Within this assumption, 125 if $L_{11}^{(1)}$ is the longitudinal integral length scale computed from $R_{u'_z u'_z}$ as defined in [28], then $l_s \approx L_{11}^{(1)}/2$. The longitudinal integral length scale $L_{11}^{(1)}$ has been computed along the jet lip-line from the large-eddy simulation [1], and serves as a reference for the calibration of equation (23). Two evaluations of formula (23) 130 along the jet lipline are presented in figure 1 for which proportionality constants of 1.0 and 2.0 are used respectively. These transversal scales l_s are compared to the reference longitudinal length scale $L_{11}^{(1)}$. As expected, the size of the structures grow linearly with the axial distance z . The slope of l_s computed for a proportionality constant of 2.0 is comparable with that of $L_{11}^{(1)}$, indicating 135 that l_s should be computed from equation (23) considering a proportionality

constant equal to 1.0.

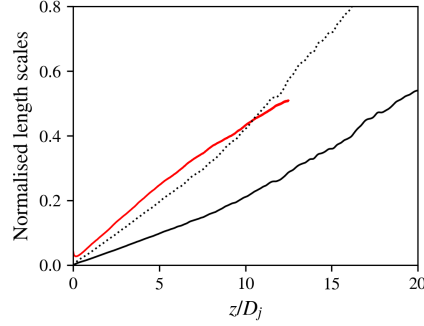


Figure 1: Evolution of the longitudinal and transversal integral length scales $L_{11}^{(1)}$ and l_s along the jet lip-line normalised by the jet diameter D_J . — reference $L_{11}^{(1)}/D_J$ directly calculated from the large-eddy flow solution for two points separated in the streamwise direction and compensated according to equation (24), — l_s/D_J rebuilt from equation (23) considering a proportionality factor set to 1.0, and l_s/D_J computed from equation (23) for a proportionality constant of 2.0.

To calibrate the amplitude \hat{q}_s of the source correlation defined in equation (20), the noise spectra radiated at $\theta_m = 90^\circ$ from the axis of a Mach number 0.9 isothermal round jet is considered. Noise spectra are expressed in dB/St, they are normalised to a distance of 1 m and corrected so as to correspond to an equivalent jet of section 1 m^2 . The Fourier transform of the pressure autocorrelation S_{pp} obtained with Tam and Auriault's formula is hence related to the normalised sound pressure level (SPL) by,

$$\text{SPL(dB/St)} = 10 \log_{10} \left(\frac{S_{pp}(\mathbf{x}_m, \omega)}{p_{\text{ref}}^2} \right) + 10 \log_{10} \left(\frac{u_j}{D_J} \right) - 10 \log_{10} \left(\frac{\pi D_J^2}{4} \right) + 10 \log_{10} (|\mathbf{x}_m|^2) \quad (25)$$

where $p_{\text{ref}} = 20.0 \mu\text{Pa}$ and $|\mathbf{x}_m|$ corresponds to the distance from the jet exhaust to the microphone position. The Strouhal number St is based on the jet diameter D_J and exhaust velocity u_j such that, $St = \omega D_J / (2\pi u_j)$. At $\theta_m = 90^\circ$ from the jet axis, mean flow refraction effects are deemed not of leading order and without external wind, Green's function appearing in Tam and Auriault's formula may

be approximated with,

$$|D_{-\mathbf{u}_0, \mathbf{x}_m}(\phi_{\mathbf{x}_m}^\dagger(\mathbf{x}, \omega))|^2 = \frac{\omega^2}{16\pi^2 a_0^4 |\mathbf{x} - \mathbf{x}_m|^2} \quad (26)$$

The derivation of this expression is provided in Appendix C. This analytical Green's function is used to evaluate the noise spectra model given in equation (18).

140 The acoustic spectra computed for $\hat{q}_s = \rho_0 k$, i.e. without fine-tuning of the amplitude of the source space-time correlation R_{QQ} , is plotted in figure 2. As previously l_s and τ_s are related through equation (21) and $l_s = \sqrt{k}/|\partial u_z/\partial r|_{\max}$ is considered. The thereby obtained noise spectra is compared in figure 2 to the spectral density computed from the LES of the Mach 0.9 round jet [14, 17, 50]
 145 that is used in this study to inform the sound source correlation R_{QQ} . This figure additionally displays two acoustic spectra measured at $\theta_m = 90^\circ$ from two Mach 0.9 isothermal round jets, one during a ECL (École Centrale de Lyon) campaign [20, 17], the other at CNRS-Pprime during the JERONIMO campaign [23, 48]. A sensible prediction in terms of level, peak frequency and width of the
 150 jet noise hump is obtained in figure 2 for the recast of Tam and Auriault's mixing noise model presented in this study. This result is all the more satisfactory as no particular tuning of the sound source parameters has been used. Note how the crudely simple free field analytical solution given in equation (26) provides a fair prediction at $\theta_m = 90^\circ$ from the jet axis [30, 47]. While the acoustic lev-
 155 els computed from the LES and that recorded at the CNRS-Pprime are closely recovered by the model, the jet investigated at ECL is 2.5 dB louder. This difference is significant, but is typical of the discrepancies that can be encountered between different acoustic test campaigns of jets presenting different nozzle-exit boundary layer states [15, 39, 70]. To enable far field acoustic measurements in
 160 directions that are upstream of the jet, the nozzle considered during the ECL test campaign has been extended by a straight conduit [20, fig.1 & fig.2] and its nozzle exit boundary layer profile differs thus from that of the two other jets. As a section of this study focusses on the acoustic field radiated upstream of the jet, noise spectra from the ECL campaign are considered in what follows.

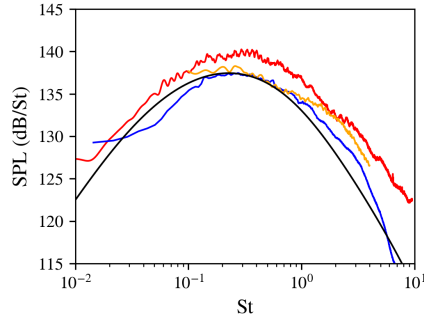


Figure 2: Acoustic spectral density at $\theta_m = 90^\circ$ from the axis of a Mach 0.9 round jet normalised to an equivalent distance of 1 m and to equivalent jet cross-section of 1 m^2 . — ECL data [20, 17], — CNRS-Pprime data [23, 48], — computed from the LES acoustic field extrapolated at a distance of $75 D_J$ from the jet axis [14, 17, 50], and, — predictions of the mixing noise model with an amplitude calibration set to 1.0.

165 3. Computation of tailored adjoint Green's functions with Actran TM

Choosing a self-adjoint operator such as Pierce's wave equation (6) to compute the radiation of sound has two major advantages. Along with ensuring the conservation of the acoustic energy, and thus preventing the development of instability waves, this feature enables the computation of adjoint solutions to
 170 Pierce's wave equation (9) by making use of the flow reversal theorem (FRT). The equivalence of both statements operators has recently been highlighted for self-adjoint operators [59]. The FRT is more handy to use than computing adjoints, since no anti-causal boundary conditions are required, only the mean-flow direction has to be reversed. This can fairly easily be achieved with some off-
 175 the-shelf solver. In this work, the frequency-domain commercial solver Actran TM is employed for that purpose.

3.1. Acoustic equation implemented in Actran TM

The finite element method solver chosen however does not solve Pierce's wave equation (6), but a linearised and normalised expression of Mörhning's equation [46]. If B is the fluctuating total enthalpy, Actran TM then considers

as dependent variable the normalised fluctuating stagnation enthalpy b , that is defined by,

$$db = \rho_{T,0} dB \quad (27)$$

where $\rho_{T,0}$ is the mean total density,

$$\rho_{T,0} = \rho_0 \left(1 + \frac{\gamma - 1}{2} \mathbf{M}_0^2 \right)^{1/(\gamma-1)} \quad (28)$$

This variable is related to the acoustic pressure p through $\partial p / \partial t = (\rho_0 / \rho_{T,0}) Db / Dt$, and Möhring's equation solved by **Actran TM** expresses then as,

$$\frac{\partial}{\partial t} \left[\frac{\rho_0}{\rho_{T,0}^2 a_0^2} \frac{Db}{Dt} \right] + \nabla \cdot \left[\frac{\rho_0 \mathbf{u}_0}{\rho_{T,0}^2 a_0^2} \frac{Db}{Dt} - \frac{\rho_0}{\rho_{T,0}^2} \nabla b \right] = S \quad (29)$$

where S is a generic sound source.

3.2. Solving Pierce's wave equation with **Actran TM**

Pierce's wave equation (6) and Möhring's equation (29) are both scalar convected wave equations. Both equations are in fact related one with another by a change of variable, and it is possible in practice to solve Pierce's wave equation (6) with **Actran TM** by preprocessing the mean-flow fields specified in input. Let $\rho_{0,C}$, $p_{0,C}$, $\mathbf{u}_{0,C}$ and $a_{0,C}$ be the customised inputs that achieve this transformation and which enable to solve Pierce's wave equation for a mean-flow given by ρ_0 , p_0 , \mathbf{u}_0 and a_0 . From a direct comparison between equations (6) and (29), it follows,

$$\mathbf{u}_{0,C} = \mathbf{u}_0, \quad a_{0,C} = a_0, \quad \text{and} \quad \frac{\rho_{0,C}}{\rho_{T,0}^2} = \frac{1}{\rho_0} \quad (30)$$

To verify these relationships, the mean flow must be preprocessed accordingly,

$$\frac{p_{0,C}}{p_0} = \frac{\rho_{0,C}}{\rho_0} = \left[1 + \frac{\gamma - 1}{2} \frac{\mathbf{u}_0^2}{a_0^2} \right]^{-2/(\gamma - 1)} \quad (31)$$

180 where it has been assumed that the mean pressure p_0 is constant. This is a very reasonable approximation for parallel flows such as jets.

This change of variable must additionally be reflected in the amplitude of the source term either prior to the computation or be compensated a posteriori

in the acoustic field computed. Let b the solution obtained with the solver when an impulsive source of unitary amplitude is considered and the preprocessing describe in equation (31) applied. The acoustic solution must then be compensated to retrieve the correct solution of Pierce's wave equation, considering,

$$\phi = \frac{i\omega}{4\pi a_{0,S}^2} \left(1 + \frac{\gamma - 1}{2} \frac{\mathbf{u}_{0,S}^2}{a_{0,S}^2} \right)^{-1/(\gamma - 1)} b^* \quad (32)$$

where b^* is the complex conjugate of b , ω the acoustic pulsation considered, $a_{0,S}$, and $\mathbf{u}_{0,S}$, the speed of sound and mean velocity evaluated at the source position. The source amplitude considered in **Actran** TM is defined with respect to the pressure (variable **AMPLITUDE_TYPE** set to **P**). Note that this correction holds for a three dimensional space, if a bidimensional configuration was studied, the amplitude correction factor, equation (32), should be multiplied by π . The implementation of this background mean flow fields reformulation has successfully been verified for a sheared and stratified propagation medium [60].

190 3.3. Computing strategy and numerical parameters chosen

The adjoint formulation relies on a sensor based description of the propagation problem, it characterises how a point in the surrounding media would radiate towards the observer location if an elementary source of sound was placed there. Thus no distributed unsteady sound sources have to be mapped on the acoustic grid, instead a delta Dirac source is set at the microphone position \mathbf{x}_m . Extending the computational domain until the microphone location would make the numerical costs prohibitive, and a strategy to solve the propagation problem for a source set out of the domain is considered therefore. The idea, illustrated in figure 3, is to separate the acoustic propagation into two regions: a numerical domain containing the meaningful part of the jet flow for which adjoint Green's function is solved numerically, and the ambient region containing the adjoint source with possibly a uniform flow. The spherical waves emitted by the adjoint source are mapped analytically on the edge of the computational domain and adjoint Green's function is solved numerically on the domain interior.

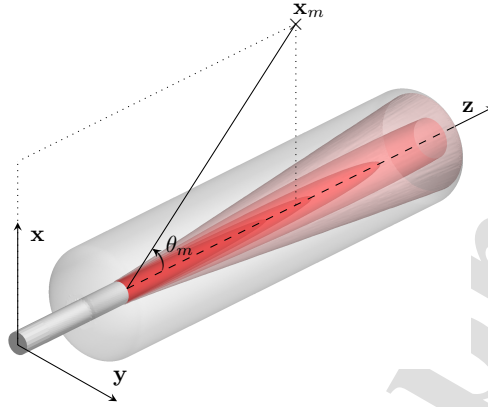


Figure 3: Schematic representation of the propagation problem and definition of the reference frame. Adjoint Green's function $\phi_{\mathbf{x}_m}^+(\mathbf{x}_s)$ is solved numerically for any \mathbf{x}_s in the light grey volume where the flow is mapped.

205 The computational aeroacoustic grid that has been set up with Actran TM's
 built-in meshing tool. The mesh obtained with elements of size $0.1D_J$ is shown
 in figure 4. The physical domain is composed by a duct of diameter D_J and
 of length $5D_J$, from the duct exhaust the domain is $20D_J$ long, and has a
 cylindrical shape with a radius of $2.5D_J$. The cylinder corners are rounded to
 210 avoid numerical singularities. The truncation of the domain is achieved with
 a $0.5D_J$ thick perfectly matched layer (PML). An additional PML region is
 added in the duct interior to simulate a semi-infinite conduit. A discussion on
 this specific **in-duct** boundary condition is given in § 5.2.

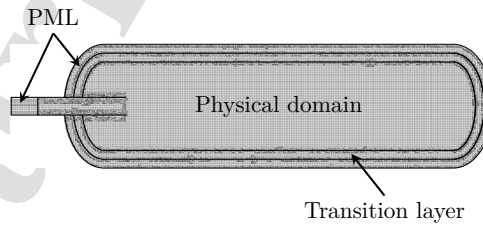


Figure 4: Slice of the computational aeroacoustic grid with elements of size $0.1D_J$.

It is not feasible to map on the boundary of the computational domain an

215 incident field from a source set outside of this domain when the exterior flow is non-uniform. A $0.5D_J$ thick transition layer is built for this reason, to interface the physical domain and the non-reflecting boundary condition. The set of variables that characterise the propagation media, namely the mean velocity \mathbf{u}_0 , the mean pressure p_0 , the mean density ρ_0 or combinations of these fields
 220 are obtained from the averaging of a large-eddy simulation [13, 14] and are mapped on the physical domain. A linear smoothing is applied on these mean flow fields for $x/D_J > 18$ and $r/D_J > 2$ so to match the uniform ambient values prescribed in the transition layer. This smoothing is visible on the Mach number field presented in figure 5. The interpolation of the turbulent kinetic energy in this domain is also shown to illustrate that this region is sufficient
 225 large to contain all the relevant sources of mixing noise. Recall that the flow reversal theorem is used to compute adjoint Green's function [59, eq. (9)], and that the mean flow fields that are mapped, have undergone the transformation described in § 3.2 and are reversed with respect to the averaged LES solution.

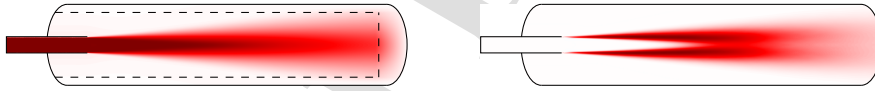


Figure 5: Averaged Mach number M_0 , and turbulent kinetic energy k computed from the large-eddy simulation and interpolated on the physical domain. $M_0 \in [0, 0.9]$ and $k \in [0, 5.6 \times 10^6]$. For $x^2 + y^2/D_J^2 \geq 4.0$ and $z/D_J \geq 18.0$ the mean velocity \mathbf{u}_0 , mean density ρ_0 and mean pressure p_0 fields are smoothly cropped to fit their ambient value.

230 Second order elements are found to enable a better cost/accuracy trade-off than first order ones [60] and are therefore considered here. To improve numerical performances, hexahedral elements are favoured over tetrahedral ones [54]. The mesh with quadratic elements of size $0.1D_J$ considered in this study possesses 7.7×10^6 degrees of freedom. Single precision is used to save half of
 235 the RAM requirements of the MUMPS solver, so that 75 GB of RAM and 6.5 h per frequencies were required to compute the solution. It is possible to chose alternative sparse system inversion algorithm with different RAM/CPU.h trade-

Size of elements	DOF	RAM requirements	Time for 100 freqs.
$0.5D_J$	0.2×10^6	1.8 GB	1.6 CPU.h
$0.2D_J$	1.7×10^6	13 GB	62 CPU.h
$0.1D_J$	7.7×10^6	75 GB	655 CPU.h
$0.075D_J$	16.2×10^6	178 GB	5500 CPU.h

Table 1: Evolution of the computation costs with the grid refinement considering quadratic elements and MUMPS solver in single precision.

offs [69]. An Intel Skylake node with 32 cores 190 GB of RAM was used with 2 parallel tasks and 16 threads on each. The computation for 100 frequencies
 240 took around 40 hours. The computation costs associated with this geometry, for different grid refinements are presented for the record in table 1.

4. Acoustic predictions at ninety degrees

Tam and Auriault's mixing noise formula is evaluated for an observer at ninety degrees from the jet axis. The reformulated expression given in equation
 245 (19) is considered. The receiver is located at a distance of $52D_J$ from the duct exit, this to mimic the acoustic far field conditions under study in [20]. The noise spectra over a Strouhal number interval ranging from 0.01 to 10 is calculated with a sampling of 100 adjoint Green's functions. Results are shown in figure 6.

250 The acoustic spectra obtained with the free field analytical solution and numerical adjoint Green's function overlap almost perfectly. Refraction effects were expected not to be of leading order at this observer angle [30, 47], but the accuracy of this match is truly remarkable. The confidence in the methodology proposed is restricted by the refinement of the aeroacoustic grid and a criteria
 255 of number of points per wavelength. From the superposition of both curves, an upper limit for the confidence interval can be estimated, and for a mesh with elements of size $0.1D_J$ a good representation of the solution can be expected up to $St \sim 4$.

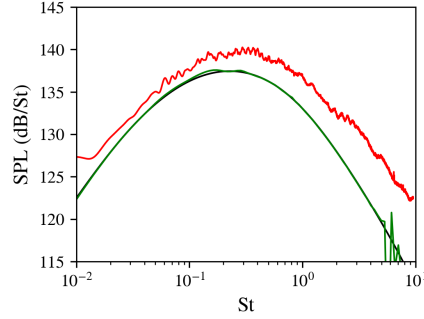


Figure 6: Acoustic predictions at $\theta_m = 90^\circ$. — measurements [20], — predictions with analytical free-field Green's function from equation (26), and, — predictions with tailored adjoint Green's functions.

The numerical solution allows to investigate in depth the behaviour of the
 260 adjoint solution. Details on the computation of the sound pressure level are
 provided here for the Strouhal numbers $St = 0.3$ and $St = 0.9$. The first value $St =$
 0.3 corresponds to the Strouhal number for which the acoustic level is maximal,
 computed solutions are reported in figure 7. To illustrate the behaviour of
 adjoint fields at higher frequency, results for $St = 0.9$ are shown in figure 8.

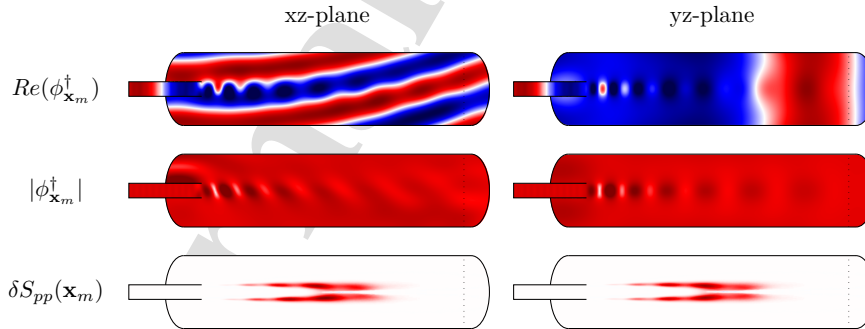


Figure 7: Real part and absolute part of adjoint Green's function $\phi_{\mathbf{x}_m}^\dagger$ for an observer at $\theta_m = 90^\circ$ and $St = 0.3$. The resulting modulation of the integrand $\delta S_{pp}(\mathbf{x}_m)$ is depicted. $Re(\phi_{\mathbf{x}_m}^\dagger) \in [-3, 3] \times 10^{-6}$ Pa.s and $|\phi_{\mathbf{x}_m}^\dagger| \in [0, 4] \times 10^{-6}$ Pa.s.

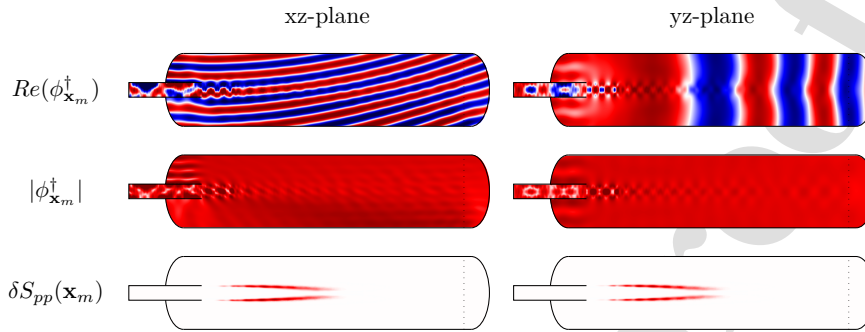


Figure 8: Real part and absolute part of adjoint Green's function $\phi_{\mathbf{x}_m}^\dagger$ for an observer at $\theta_m = 90^\circ$ and $St = 0.9$. The resulting modulation of the integrand $\delta S_{pp}(\mathbf{x}_m)$ is depicted. $Re(\phi_{\mathbf{x}_m}^\dagger) \in [-3, 3] \times 10^{-6}$ Pa.s and $|\phi_{\mathbf{x}_m}^\dagger| \in [0, 4] \times 10^{-6}$ Pa.s.

265 These figures present visualisations in different cross-sections of the real part and the absolute part of adjoint Green's function $\phi_{\mathbf{x}_m}^\dagger$. The integrand $\delta S_{pp}(\mathbf{x}_m)$ of Tam and Auriault's formula, as given by equation (19), is also reproduced for these Strouhal numbers. It is the projection of adjoint Green's function on the turbulent mixing noise source model. In other words, this function
 270 filters the energy of the sound source by selecting the part that radiates toward the observer in weighting this contribution to include the acoustic propagation effects. Adjoint Green's function $\phi_{\mathbf{x}_m}^\dagger(\mathbf{x})$ accounts for all the propagation effects and indicates how effectively a source put in \mathbf{x} would radiate to the observer \mathbf{x}_m , while $\delta S_{pp}(\mathbf{x}_m)$ represents the actual contribution at the observer position of the
 275 sound source. Note that within the present framework, sound generation and sound propagation are genuinely decoupled. In this sense the adjoint method shares the mindset of acoustic analogies and offers an interesting extension to the latter theory [25].

Even though it is seen in figure 6 that the acoustic noise spectra computed
 280 using tailored adjoint Green's functions closely follows the one obtained with free field analytical Green's functions, numerical Green's functions depicted in figures 7 and 8 present substantial differences with regard to their simplified analytical counterparts. This is most easily observed by considering the absolute

values of both sets of Green's functions, and by recalling that from equation (26) the amplitude of the analytical solutions is roughly constant over the physical domain for an adjoint source set in the far field. An acoustic mode confined in the jet plume is clearly identified in figures 7 and 8, leading to a modulation of the integrand $\delta S_{pp}(\mathbf{x}_m)$ that is the scalar product of adjoint Green's function with the source term. Surprisingly enough, for the two Strouhal numbers considered and for this simple jet, $St= 0.3$ and $St= 0.9$, the acoustic energy received at ninety degrees from the jet axis originates slightly more from the shear layer area masked by the jet flow than from the area directly facing the observation point. The presence of the duct surface and the jet flow induce a scattered field. These results are reproduced for observers located at $\theta_m = 30^\circ$ and $\theta_m = 150^\circ$, and presented in Appendix D for the same Strouhal numbers values $St= 0.3$ and $St= 0.9$.

Discussing in details these adjoint solutions would go beyond the scope of this study which targets at presenting a methodology based on a stable formulation to compute sound propagation, and to calculate tailored adjoint Green's functions to predict jet noise. Note merely that the scalar product of adjoint Green's function on a sound source a priori as considered in this approach explicitly provides the actual contribution of a source of sound to a given observer location. With respect to previous formulations, the adjoint fields are easily accessible and computed in a robust manner. Note also that modal structures in the jet plume are almost absent for an observer located at $\theta_m = 30^\circ$, they are visible at $\theta_m = 90^\circ$ and very strong for an observer located upstream at $\theta_m = 150^\circ$. What is more, the projection of these adjoint Green's functions on the sound source model makes clearly visible that various parts of the shear layer contribute at different observer angle.

5. Acoustic predictions in the upstream direction

Tailored adjoint Green's functions or analytically known free field Green's functions provide nearly identical predictions at ninety degrees. To illustrate the

improvements in the predictions that can result from the use of tailored adjoint Green's functions, acoustic spectra computed at $\theta_m = 150^\circ$ are presented. At this shallow angle, the emergence of tones in the acoustic far field spectrum has been reported and receive, since recently, a special attention in the literature [68, 14, 17, 71]. It has been shown that these tones are related to the existence of guided jet waves inside the jet flow, and that despite their strong intensity, they are of purely acoustic nature.

Predictions obtained with the proposed model in considering numerical and analytical adjoint Green's functions computed over a sample of 200 Strouhal numbers are plotted in figure 9. The interested reader will find in Appendix D and in Appendix E visualisations of some tailored adjoint Green's functions which have been used for this calculation. The noise predictions are compared against the far field noise spectra measured for a Mach 0.9 isothermal round jet during the ECL test campaign[17]. Six tones are clearly visible in the sound pressure level calculated from the experiment at this grazing upstream angle. They are qualitatively reproduced in the prediction based on tailored adjoint Green's functions and absent from the noise spectra relying on the free field propagation model, indicating thereby that the tones are associated with purely sound propagation effects.

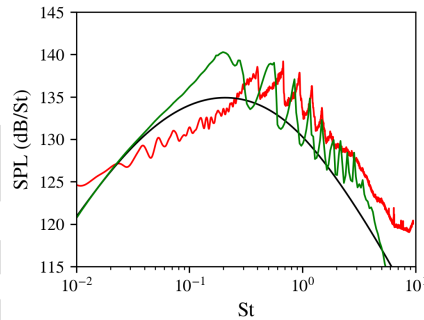


Figure 9: Acoustic predictions at $\theta_m = 150^\circ$. — red — measurements [20], — black — predictions considering free field adjoint Green's function, and, — green — predictions with tailored adjoint Green's functions.

The amplitude of the tones are properly captured by the model within 2 dB. The first peak computed with tailored adjoint Green's functions is overestimated, while the third, the fourth and the fifth peak are a slightly underestimated. Above the frequency of the first tone, the broadband level of the acoustic spectra predicted is lower than the measured one, leading to higher peak-to-peak amplitudes in the prediction. It is seen in figure 9, that the most significant flaw in the prediction lies in the frequencies of the tones computed that are systematically lower than the measured ones. This point is addressed in what follows.

5.1. Influence of the flow and the geometry

Guided jet waves were first identified as the neutral wave modes of the jet. Tam and Ahuja [61] have shown that their mode shape as well as their frequency are correctly predicted by a cylindrical vortex sheet model. In order to get closer to the assumptions of their model, and attempt thereby to retrieve the correct tone frequencies, tailored adjoint Green's functions are computed for the two additional configurations displayed in figure 10. Figure 10 (a) represents the base flow considered in previous calculations. The configuration shown in figure 10 (b) models the jet flow with a cylindrical plug flow exhausting from the semi-infinite straight duct. As in figure 10 (a), the base flow in figure 10 (b) is gradually restored to ambient values to enable a truncation of the numerical domain with minimal reflection at the boundary. A cylindrical plug flow with no solid surface that aims at best reproducing the hypothesis of the vortex sheet model is considered in figure 10 (c). For this last configuration, the truncation of the numerical domain is achieved with three independent PML mapped with uniform flows.

Acoustic spectra at $\theta_m = 150^\circ$ computed for these configurations over a sample of 200 Strouhal numbers are presented in figure 11. In all configurations, the sound sources are modelled identically to those of previous calculations, and hence, only the presence or absence of the pipe, the base flow, and the associated propagation effects differ in these computations. The prediction obtained for the

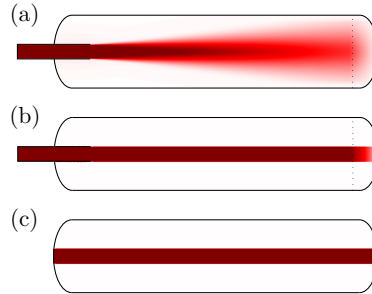


Figure 10: Mach number M_0 considered for the computations of tailored adjoint Green's functions. The cases (a) and (b) include a portion of straight duct, from $z/D_J = 18.0$ downstream of the jet exhaust the mean flow is smoothed to ambient value. In (b) and (c), a plug flow with an infinitely thin shear layer is considered to fit into the assumption of the vortex sheet model. $M_0 \in [0, 0.9]$.

case (a) is identical to the one presented figure 9 and reproduced for comparison. The acoustic results obtained with the infinitely thin shear layer model, the cases (b) and (c), are quite similar. The amplitude of the first three peaks
 365 increased with respect to the reference spectra corresponding to the case (a) as well as the peak-to-peak amplitude that is larger than 15 dB for cases (b) and (c). The tones are narrower, and the broadband level is more than 5 dB less energetic compared to the reference spectra. The reason for this substantial decrease of the broadband level is found in the recast of Tam and Auriault's
 370 model, in equations (18) and (19), for which the exponential in the integrand filters out any contribution of the sound source when $u_0 \rightarrow 0$. That is for the plug flow of case (b) and (c), only the part of the sound source in the flow effectively contribute to the total sound pressure level. It is however seen from figure 11, that the position of the peaks are not significantly modified,
 375 indicating a fairly high robustness of the peak position with respect to the jet flow profile [14] and geometry. Adjoint Green's functions tailored to these three configurations are presented in Appendix E, and their structure for the first three tones are also briefly discussed. It comes out, that the length of the jet potential core, the shear layer thickness as well as the presence of the nozzle are

380 not sufficient to recover the correct frequencies of the tones.

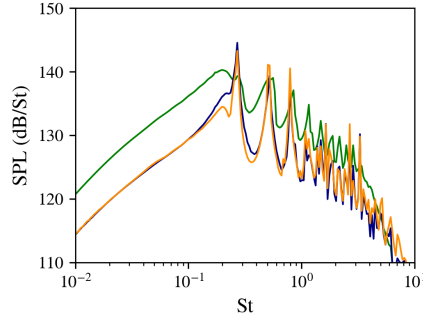


Figure 11: Acoustic predictions at $\theta_m = 150^\circ$ for the configurations presented in figure 10. — case (a), — case (b), and, — case (c).

5.2. Influence of the *in-duct* boundary condition

Acoustic modes in the jet plume are visible in tailored adjoint Green's functions computed for observers located in the upstream direction. This is illustrated in Appendix E for an observer at $\theta_m = 150^\circ$. At the conduit exhaust
 385 these modal structures interface with the duct modes, so that an influence of the nozzle impedance on adjoint Green's function computed in the jet potential core can be expected.

So far, the duct has been modelled as semi-infinite by considering a PML, and the value of the reflection coefficient in the duct is low. This contrasts with
 390 laboratory tests for which ducts have finite length, and are reflective. This reflection in the conduit needs to be accounted for in the global stability analysis of trapped acoustic modes as shown by Schmidt *et al.* [55, Appendix B] to retrieve the correct envelope of the least damped global mode. It is moreover known that changing a non-reflecting boundary condition to a partially reflect-
 395 ing one shifts the eigenfrequencies of resonators [57], and a modification of the nozzle impedance may influence the tone frequencies of upstream-propagating guided jet modes in a similar fashion.

Since the nozzle impedance is unknown, a simple hard-wall boundary condition ($u'_z = 0$) that is permeable to the flow ($u_{0,z} \neq 0$) is considered in what follows to mimic the finite duct length and its internal reflection. Figure 12 (a) compares the acoustic prediction obtained with the semi-infinite duct model and the one assuming a finite length duct. Taking into account the duct internal reflection as for an effect to increase slightly the tone frequencies and to widen the peaks. With respect to the predictions obtained with the semi-infinite duct model, the falling edge of the tone occurs for a Strouhal number increased by roughly 0.1, but the rising edge of the tone is unchanged. The amplitude of the peaks remain globally identical, except for the fifth peak that is increased by approximately 3 dB. The sound pressure level minima between the peaks are also 3-5 dB more energetic. For Strouhal numbers lower than $St = 0.4$, the acoustic spectra presents series of peaks, the frequency of which are harmonics of the quarter wave resonator formed by the duct cavity [27]. Experiments on the acoustic resonance of an open-ended duct [37] have shown that such resonances of a duct in flow are almost completely suppressed by losses when the flow Mach number exceeds $M = 0.4$. To remove these peaks, three computations with ducts of length D_J , $2D_J$ and $5D_J$ are considered, and their acoustic spectra averaged. Figure 12 (b) displays the thereby obtained averaged acoustic spectra as well as the three individual predictions made for that purpose. The tones identified previously as guided jet waves are not significantly altered, while the other events associated with the duct resonance are smoothed. In addition, the amplitude of the fifth tone returned to a level similar to the one obtained with a semi-infinite duct model.

This acoustic spectra obtained from averaging of the predictions computed for different duct lengths gives an estimate of the sound pressure level that would be obtained if the duct internal reflection would be accounted for in the sound propagation. Figure 13 compares this acoustic spectra with measurements and predictions that consider the duct as semi-infinite. Predictions associated with a free field propagation of Tam and Auriault's mixing noise are given for the record. The tone frequencies predicted by accounting for the **in-duct** reflec-

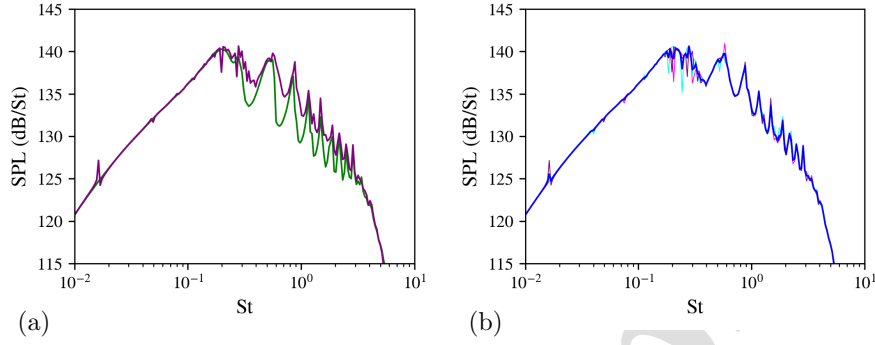


Figure 12: Acoustic predictions at $\theta_m = 150^\circ$. (a), predictions — with the semi-infinite duct model, and — with a fully reflective duct of length $5D_J$. (b), predictions with a fully reflective duct, —, of length D_J , —, of length $2D_J$, and, —, of length $5D_J$. —, noise spectra computed from the averaging of the three predictions with different duct length.

430 tions matches now much better with the measured ones. The noise spectra computed by accounting for **in-duct** reflections is also systematically louder than the solution considering free field propagation. For the semi-infinite duct model, minima between peaks are lower than their counterpart that assume free field propagation, suggesting that some acoustic energy possibly leaks out through the duct at these frequencies.

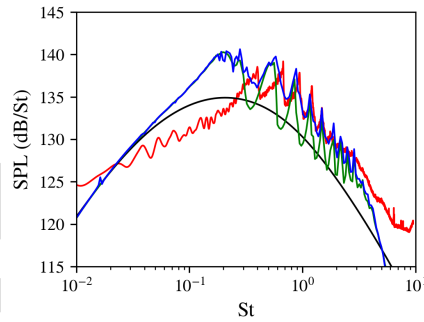


Figure 13: Acoustic predictions at $\theta_m = 150^\circ$. —, measurements [20], —, predictions assuming the duct is semi-infinite, —, predictions modelling the duct internal reflection, and —, predictions with analytical free-field Green's function from equation (26).

435 6. Far field acoustic spectra with a duct of finite length

The effect of accounting for **in-duct** reflections is now investigated for other polar angles. Figure 14 presents the acoustic spectra computed for observers located at angles from $\theta_m = 30^\circ$ to $\theta_m = 140^\circ$. As previously, to remove the non-physical duct quarter wave resonances, adjoint Green's functions are
 440 computed in assuming a total **in-duct** reflection of the acoustics for three duct lengths. An averaging of the resulting spectra is then considered.

The emergence of guided jet waves are visible for the predictions that consider tailored adjoint Green's functions at the polar angles $\theta_m = 120^\circ$, $\theta_m = 130^\circ$ and $\theta_m = 140^\circ$, which are displayed in figures 14 (d) to (f). At these angles
 445 the dynamic of the tones are correctly predicted within a tolerance of 3 dB for a decade of Strouhal number between $St = 0.2$ and $St = 2.0$. The tones are about 5 dB more energetic when **in-duct** reflections are modelled, and, as for previous computation at $\theta_m = 150^\circ$, their position is also better predicted when **in-duct** reflections are modelled. This confirms the importance of accounting
 450 for the nozzle impedance to correctly predict these events.

Although the model is reasonably successful in capturing noise levels above $\theta_m = 120^\circ$ in this decade of Strouhal number, the predicted spectra underestimate the measurements as the observer moves away from these angles. At $\theta_m = 90^\circ$, measured levels are under-predicted by 2 dB, at $\theta_m = 60^\circ$, 5 dB are
 455 missing, and at $\theta_m = 30^\circ$, the gap is as large as 17 dB. The downstream polar angles are dominated by the radiation of large turbulent scales [64] which are not included in Tam and Auriault's mixing noise model. Thus it is not surprising that the model fails at predicting the correct amplitudes at these angles. A more complete modelling of the Reynolds stress tensor than that of equation
 460 (7) seems also able to consistently retrieve the correct polar directivity [53, 3]. Investigating alternative noise source models [31, 42, 4] may thus correct this trend.

At $\theta_m = 130^\circ$, $\theta_m = 140^\circ$ and $\theta_m = 150^\circ$, the low frequency spectra is over-estimated independently of the sound propagation model considered indicating

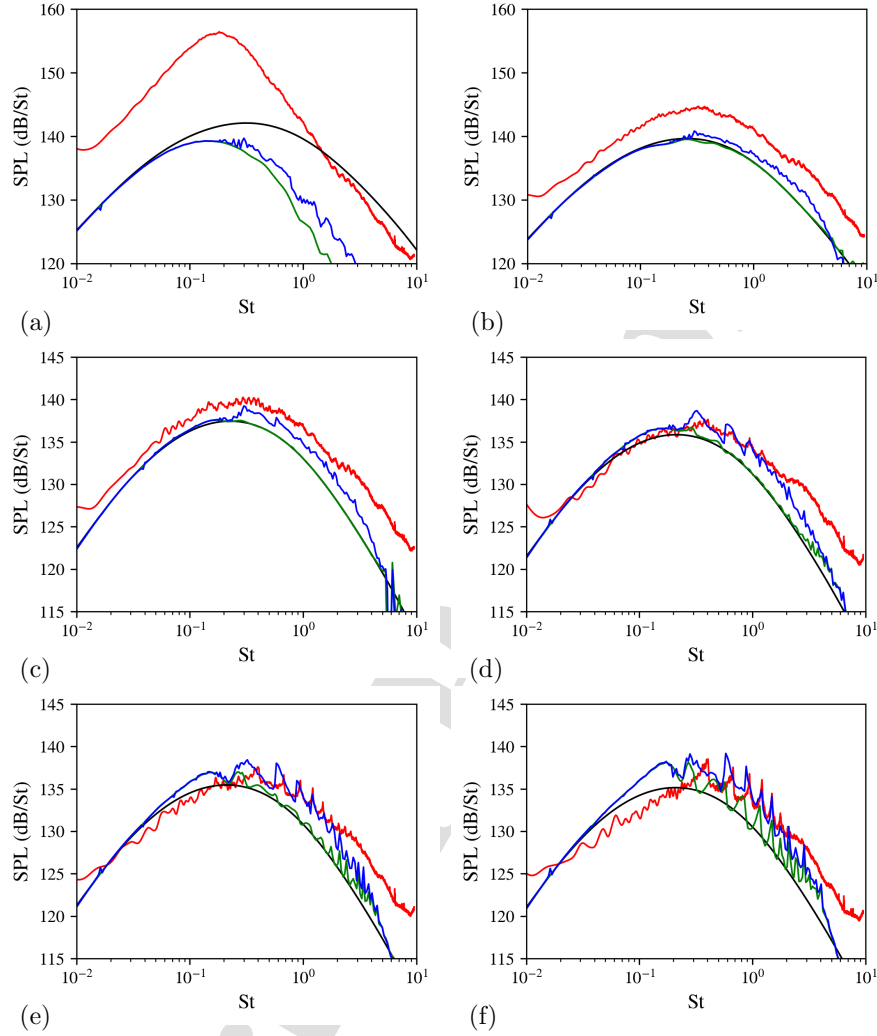


Figure 14: Acoustic predictions at, (a) $\theta_m = 30^\circ$, (b) $\theta_m = 60^\circ$, (c) $\theta_m = 90^\circ$, (d) $\theta_m = 120^\circ$, (e) $\theta_m = 130^\circ$ and (f) $\theta_m = 140^\circ$. —, measurements [20], —, predictions assuming the duct is semi-infinite, —, predictions modelling the duct internal reflection, and —, predictions with analytical free-field Green's function from equation (26).

465 an imperfection of the model proposed here. At these upstream shallow angles, a hump centred around $St = 0.1$ emerges in the noise spectra computed from tailored Green's functions. The latter is predicted equally by modelling the duct

as semi-infinite or as totally reflecting, but it is absent from the measurements and from the predictions that assume free field propagation. The amplitude of
 470 this peak increases as the observer moves upstream and that it finally merges with the first tone of the upstream-propagating guided jet wave. The origin of this phenomena is presently unknown and deserves further investigation.

At $\theta_m = 30^\circ$, the acoustic spectrum computed considering tailored adjoint Green's functions are significantly narrower than their free field counterpart.
 475 This is a well-known consequence of acoustic refraction, yet what is remarkable is that the shape of the $\theta_m = 30^\circ$ degree measured spectrum is thereby retrieved. Noise spectra computed without modelling **in-duct** reflections closely follow the predictions achieved with the free field analytical model from $\theta_m = 60^\circ$ to $\theta_m = 130^\circ$ in a noteworthy way. All acoustic predictions overlap for Strouhal
 480 numbers lower than $St = 0.1$. Above this threshold, predictions are sensitive to the methodology used to propagate sound. It is seen that the acoustic predictions that account for **in-duct** reflections are systematically more energetic than those obtained with a semi-infinite duct model. For Strouhal numbers greater than $St = 0.3$, this extra acoustic energy is spread over more than one
 485 decade of Strouhal number, and is of the order of 2-3 dB. This amount of energy is considerable.

7. Conclusion

This study reformulates Tam and Auriault's mixing noise model for Pierce's wave equation, and solves numerically adjoint Green's functions associated with
 490 the jet noise propagation problem. The benefits of this new formulation are twofold; the acoustic propagation problem is made unconditionally stable and the adjoint solution to the propagation problem can be solved using the convenient flow reversal theorem. The commercial solver **Actran**™ is used to compute adjoint Green's functions that are tailored to the geometry and the
 495 flow of the subsonic jet under consideration. Noise predictions with a reasonably fine frequency discretisation are obtained in computing time of the order

of one day.

Within a noise prediction strategy based on acoustic analogies, there are features related to sound propagation in jets, such as upstream propagating guided jet waves, that tailored adjoint Green's functions can describe with some success. Deviations have been observed between the frequencies of the tones measured and those predicted assuming a semi-infinite duct model. Investigations at constant jet Mach number have shown that the position of these peaks are not very sensitive to the structure of the jet plume, but are strongly influenced by the impedance of the conduit. Considering a total reflection of the acoustic energy in the duct broadens the descending fronts of the tone associated with the jet neutral mode, and give peak positions more in line with what is measured.

Tam and Auriault's prediction model for turbulent mixing noise is unable to describe the acoustic directivity in the downstream direction, but encounters also limitations in the upstream arc. Effort in consistently redrafting a noise source model can be undertaken, now that some confidence is gained in the computation of sound propagation effects with help of tailored adjoint Green's functions. An effort will be made to address this specific point.

In an acoustic analogy framework, the radiating part of the sound source is filtered by Green's functions. The adjoint isolates this contribution and weights the source intensity by taking into account the acoustic path from the source to the listener. Starting from a source model, the adjoint allows to characterise its contribution to the sound received by a given observer, and thus, gives indication on the localisation of the radiating part of sound sources. It is seen that the way in which shear layers radiate depends on the point of observation. At some frequencies, the sound field which radiates downstream of the jet does not pass through the jet, but comes mainly from the shear layer that is directly visible from the observation point. Upstream, the opposite is true, adjoint Green's functions indicates that it is more the part of the shear layer hidden by the jet that contributes to the listener position.

Acknowledgements

The authors would like to thank César Legendre for his expert and constant support in setting up the calculations in Actran TM. The first author benefited from insightful discussions on the physics of guided jet modes with Mathieu Varé. This work was performed within the framework of the AMBROSIA project founded by The French Civil Aviation Authority (DGAC Convention 2019-18), with also the support of the Labex CeLyA of the Université de Lyon, within the programme "Investissements d'Avenir" (ANR-10-LABX-0060/ANR-16-IDEX-0005) operated by the French National Research Agency (ANR). This work was granted access to the HPC resources of PMCS2I (Pôle de Modélisation et de Calcul en Sciences de l'Ingénieur de l'Information) of École Centrale de Lyon.

Appendix A. Conventions and formulae

Appendix A.1. Definition of the pressure autocorrelation

The pressure autocorrelation $R_{pp}(\mathbf{x}_m, \tau)$ at a position \mathbf{x}_m and for a time separation τ is by definition, $R_{pp}(\mathbf{x}_m, \tau) \equiv \overline{p(\mathbf{x}_m, \bullet)p(\mathbf{x}_m, \bullet + \tau)}$, with,

$$\overline{p(\mathbf{x}_m, \bullet)p(\mathbf{x}_m, \bullet + \tau)} = \lim_{T \rightarrow \infty} \frac{1}{T} \int_{-T/2}^{T/2} dt_m p(\mathbf{x}_m, t_m) p(\mathbf{x}_m, t_m + \tau) \quad (\text{A.1})$$

Appendix A.2. Convention for the Fourier transform

A non-unitary Fourier transform in time is considered in this study,

$$F(\mathbf{x}, \omega) = \int_{\mathbb{R}} dt f(\mathbf{x}, t) e^{i\omega t} \quad \text{and} \quad f(\mathbf{x}, t) = \frac{1}{2\pi} \int_{\mathbb{R}} d\omega F(\mathbf{x}, \omega) e^{-i\omega t} \quad (\text{A.2})$$

Source-observer Green's function is defined in the frequency domain as $G_{\mathbf{x}_s}^{(\mathbf{x}_m, \omega)}$ and in the time domain as $g_{\mathbf{x}_s, t_s}^{(\mathbf{x}_m, t_m)} \equiv g_{\mathbf{x}_s}^{(\mathbf{x}_m, \tau)}$, with $\tau \equiv t_m - t_s$. The time Fourier transform definition for Green's function chosen for this study writes,

$$G_{\mathbf{x}_s}^{(\mathbf{x}_m, \omega)} = \int_{\mathbb{R}} d\tau g_{\mathbf{x}_s}^{(\mathbf{x}_m, \tau)} e^{i\omega\tau} = \int_{\mathbb{R}} d\tau g_{\mathbf{x}_s, t_s}^{(\mathbf{x}_m, t_s + \tau)} e^{i\omega\tau} \quad (\text{A.3})$$

and,

$$g_{\mathbf{x}_s, t_s}^{(\mathbf{x}_m, t_m)} = g_{\mathbf{x}_s}^{(\mathbf{x}_m, \tau)} = \frac{1}{2\pi} \int_{\mathbb{R}} d\omega G_{\mathbf{x}_s}^{(\mathbf{x}_m, \omega)} e^{-i\omega\tau} \quad (\text{A.4})$$

Appendix A.3. Choice of the scalar product

The scalar product of two real valued vectors \mathbf{a} and \mathbf{b} is defined on a space Ω as,

$$\langle \mathbf{a}, \mathbf{b} \rangle = \int_{\Omega} d\mathbf{x} \int_{\mathbb{R}} dt \mathbf{a}(\mathbf{x}, t) \cdot \mathbf{b}(\mathbf{x}, t) \quad (\text{A.5})$$

Appendix A.4. Integration formulae

The reformulation of Tam and Auriault's mixing noise model has recourse to the following formulas.

For $Re(\mu) > 0$,

$$\int_{\mathbb{R}} dx \exp(-\mu x^2) = \sqrt{\frac{\pi}{\mu}} \quad (\text{A.6})$$

$$\int_{\mathbb{R}} dx x \exp(-\mu x^2) = 0 \quad (\text{A.7})$$

For $Re(\mu) + Im(\nu) > 0$,

$$\int_{\mathbb{R}} dx \exp(-\mu|x| + i\nu x) = \frac{1}{\mu - i\nu} + \frac{1}{\mu + i\nu} = \frac{2\mu}{\mu^2 + \nu^2} \quad (\text{A.8})$$

$$\int_{\mathbb{R}} dx x \exp(-\mu|x| + i\nu x) = \frac{1}{(\mu - i\nu)^2} - \frac{1}{(\mu + i\nu)^2} = \frac{4i\mu\nu}{(\mu^2 + \nu^2)^2} \quad (\text{A.9})$$

Integral computation found in [35, eq. (3.323), p.337 in 7th ed.] for $Re(p^2) > 0$,

$$\int_{\mathbb{R}} dx \exp(-p^2 x^2 \pm qx) = \frac{\sqrt{\pi}}{p} \exp\left(\frac{q^2}{4p^2}\right) \quad (\text{A.10})$$

Appendix B. Details on the derivations

This section presents the details of the reformulation of Tam and Auriault's mixing noise model, where, for the sake of concision, the pressure autocorrelation R_{pp} is considered as starting point instead of its Fourier transform S_{pp} .

Appendix B.1. Calculation of the acoustic noise spectra

The pressure autocorrelation expressed with Pierce's wave equation writes,

$$R_{pp}(\mathbf{x}_m, \tau) = \frac{\overline{D(\phi)} \overline{D(\phi)}}{D_{\bullet, \mathbf{x}_m} D_{\bullet + \tau, \mathbf{x}_m}} \quad (\text{B.1})$$

or more explicitly,

$$R_{pp}(\mathbf{x}_m, \tau) = \lim_{T \rightarrow \infty} \frac{1}{T} \int_{-T/2}^{T/2} dt_m \frac{D(\phi)}{D_{t_m, \mathbf{x}_m}} \frac{D(\phi)}{D_{t_m + \tau, \mathbf{x}_m}} \quad (\text{B.2})$$

Recasting ϕ with Lagrange's identity furnishes,

$$R_{pp}(\mathbf{x}_m, \tau) = \lim_{T \rightarrow \infty} \frac{1}{T} \int_{-T/2}^{T/2} dt_m \frac{D}{D_{t_m, \mathbf{x}_m}} \left[\int_{\Omega} d\mathbf{x}_1 \int_{\mathbb{R}} dt_1 \phi_{\mathbf{x}_m, t_m}^{\dagger}(\mathbf{x}_1, t_1) \frac{D(q_s(\mathbf{x}_1, t_1))}{D_{t_1, \mathbf{x}_1}} \right] \\ \frac{D}{D_{t_m + \tau, \mathbf{x}_m}} \left[\int_{\Omega} d\mathbf{x}_2 \int_{\mathbb{R}} dt_2 \phi_{\mathbf{x}_m, t_m + \tau}^{\dagger}(\mathbf{x}_2, t_2) \frac{D(q_s(\mathbf{x}_2, t_2))}{D_{t_2, \mathbf{x}_2}} \right] \quad (\text{B.3})$$

Because τ is constant with respect to t_m , $D/D_{t_m + \tau, \mathbf{x}_m} = D/D_{t_m, \mathbf{x}_m}$, moreover \mathbf{x}_1 , \mathbf{x}_2 , t_1 and t_2 are independent of \mathbf{x}_m and t_m , so that previous material derivatives only applies on the ϕ^{\dagger} fields leading to,

$$R_{pp}(\mathbf{x}_m, \tau) = \lim_{T \rightarrow \infty} \frac{1}{T} \int_{-T/2}^{T/2} dt_m \int_{\Omega} d\mathbf{x}_1 \int_{\Omega} d\mathbf{x}_2 \int_{\mathbb{R}} dt_1 \int_{\mathbb{R}} dt_2 \frac{D\left(\phi_{\mathbf{x}_m, t_m}^{\dagger}(\mathbf{x}_1, t_1)\right)}{D_{t_m, \mathbf{x}_m}} \frac{D\left(\phi_{\mathbf{x}_m, t_m + \tau}^{\dagger}(\mathbf{x}_2, t_2)\right)}{D_{t_m, \mathbf{x}_m}} \\ \frac{D(q_s(\mathbf{x}_1, t_1))}{D_{t_1, \mathbf{x}_1}} \frac{D(q_s(\mathbf{x}_2, t_2))}{D_{t_2, \mathbf{x}_2}} \quad (\text{B.4})$$

Recalling the equivalent notation for the Green functions, $G_{\mathbf{x}_s, t_s}(\mathbf{x}_m, t_m) \equiv G_{\mathbf{x}_s}(\mathbf{x}_m, t_m - t_s)$, and applying to t_1 and t_2 the change of variable $\tilde{t}_1 \equiv t_1 - t_m$ and $\tilde{t}_2 \equiv t_2 - t_m$ gives,

$$R_{pp}(\mathbf{x}_m, \tau) = \lim_{T \rightarrow \infty} \frac{1}{T} \int_{-T/2}^{T/2} dt_m \int_{\Omega} d\mathbf{x}_1 \int_{\Omega} d\mathbf{x}_2 \int_{\mathbb{R}} d\tilde{t}_1 \int_{\mathbb{R}} d\tilde{t}_2 \frac{D\left(\phi_{\mathbf{x}_m}^{\dagger}(\mathbf{x}_1, \tilde{t}_1)\right)}{D_{t_m, \mathbf{x}_m}} \\ \frac{D\left(\phi_{\mathbf{x}_m}^{\dagger}(\mathbf{x}_2, \tilde{t}_2 - \tau)\right)}{D_{t_m, \mathbf{x}_m}} \frac{D(q_s(\mathbf{x}_1, \tilde{t}_1 + t_m))}{D_{\tilde{t}_1 + t_m, \mathbf{x}_1}} \frac{D(q_s(\mathbf{x}_2, \tilde{t}_2 + t_m))}{D_{\tilde{t}_2 + t_m, \mathbf{x}_2}} \quad (\text{B.5})$$

Due to the time-shift invariance of $\phi_{\mathbf{x}_m}^\dagger$, their material derivatives can be expressed as function of \tilde{t}_1 and \tilde{t}_2 ,

$$\begin{aligned} \frac{\partial}{\partial t_m} \phi_{\mathbf{x}_m}^\dagger(\mathbf{x}_1, \tilde{t}_1) &= \frac{\partial}{\partial t_m} \phi_{\mathbf{x}_m}^\dagger(\mathbf{x}_1, t_1 - t_m) \\ &= -\frac{\partial}{\partial(t_1 - t_m)} \phi_{\mathbf{x}_m}^\dagger(\mathbf{x}_1, t_1 - t_m) \\ &= -\frac{\partial}{\partial \tilde{t}_1} \phi_{\mathbf{x}_m}^\dagger(\mathbf{x}_1, \tilde{t}_1) \end{aligned} \quad (\text{B.6})$$

and similarly,

$$\frac{\partial}{\partial t_m} \phi_{\mathbf{x}_m}^\dagger(\mathbf{x}_2, \tilde{t}_2 - \tau) = -\frac{\partial}{\partial \tilde{t}_2} \phi_{\mathbf{x}_m}^\dagger(\mathbf{x}_2, \tilde{t}_2 - \tau) \quad (\text{B.7})$$

Since \tilde{t}_1 and \tilde{t}_2 are independent of t_m the pressure time autocorrelation R_{pp} rewrites as,

$$\begin{aligned} R_{pp}(\mathbf{x}_m, \tau) &= \int_{\Omega} d\mathbf{x}_1 \int_{\Omega} d\mathbf{x}_2 \int_{\mathbb{R}} d\tilde{t}_1 \int_{\mathbb{R}} d\tilde{t}_2 \frac{D\left(\phi_{\mathbf{x}_m}^\dagger(\mathbf{x}_1, \tilde{t}_1)\right)}{D_{-\tilde{t}_1, \mathbf{x}_m}} \frac{D\left(\phi_{\mathbf{x}_m}^\dagger(\mathbf{x}_2, \tilde{t}_2 - \tau)\right)}{D_{-\tilde{t}_2, \mathbf{x}_m}} \\ &\quad \lim_{T \rightarrow \infty} \frac{1}{T} \int_{-T/2}^{T/2} dt_m \frac{D(q_s(\mathbf{x}_1, \tilde{t}_1 + t_m))}{D_{t_m, \mathbf{x}_1}} \frac{D(q_s(\mathbf{x}_2, \tilde{t}_2 + t_m))}{D_{t_m, \mathbf{x}_2}} \end{aligned} \quad (\text{B.8})$$

Eventually, the change of variables $\tilde{t}_m \equiv t_m + \tilde{t}_2$ and $\tilde{\tau} \equiv \tilde{t}_1 - \tilde{t}_2 = t_1 - t_2$ allows to retrieve the Q -term space-time correlation R_{QQ} defined as,

$$R_{QQ}(\mathbf{x}_1, \mathbf{x}_2, \tilde{\tau}) \equiv \lim_{T \rightarrow \infty} \frac{1}{T} \int_{-T/2}^{T/2} d\tilde{t}_m \frac{D(q_s(\mathbf{x}_1, \tilde{t}_m + \tilde{\tau}))}{D_{\tilde{t}_m, \mathbf{x}_1}} \frac{D(q_s(\mathbf{x}_2, \tilde{t}_m))}{D_{\tilde{t}_m, \mathbf{x}_2}} \quad (\text{B.9})$$

or with an alternative notation,

$$R_{QQ}(\mathbf{x}_1, \mathbf{x}_2, \tilde{\tau}) \equiv \frac{D(q_s(\mathbf{x}_1, \bullet + \tilde{\tau}))}{D_{\bullet, \mathbf{x}_1}} \frac{D(q_s(\mathbf{x}_2, \bullet))}{D_{\bullet, \mathbf{x}_2}} \quad (\text{B.10})$$

As previously, the Fourier transformed pressure autocorrelation S_{pp} can be computed, and after decomposing in the Fourier space the material derivatives

of $\phi_{\mathbf{x}_m}^\dagger$, i.e.

$$\begin{aligned} \frac{D\left(\phi_{\mathbf{x}_m}^\dagger(\mathbf{x}_1, \tilde{t}_1)\right)}{D_{-\tilde{t}_1, \mathbf{x}_m}} &= \int_{\mathbb{R}} \frac{d\omega_1}{2\pi} \left(i\omega_1 \phi_{\mathbf{x}_m}^\dagger(\mathbf{x}_1, \omega_1) + \mathbf{u}_0 \cdot \nabla \phi_{\mathbf{x}_m}^\dagger(\mathbf{x}_1, \omega_1) \right) e^{-i\omega_1 \tilde{t}_1} \\ &= - \int_{\mathbb{R}} \frac{d\omega_1}{2\pi} D_{-\mathbf{u}_0, \mathbf{x}_m} \left(\phi_{\mathbf{x}_m}^\dagger(\mathbf{x}_1, \omega_1) \right) e^{-i\omega_1 \tilde{t}_1} \end{aligned} \quad (\text{B.11})$$

in a similar fashion,

$$\frac{D\left(\phi_{\mathbf{x}_m}^\dagger(\mathbf{x}_2, \tilde{t}_2 - \tau)\right)}{D_{-\tilde{t}_2, \mathbf{x}_m}} = - \int_{\mathbb{R}} \frac{d\omega_2}{2\pi} D_{-\mathbf{u}_0, \mathbf{x}_m} \left(\phi_{\mathbf{x}_m}^\dagger(\mathbf{x}_2, \omega_2) \right) e^{-i\omega_2(\tilde{t}_2 - \tau)} \quad (\text{B.12})$$

where $D_{\mathbf{u}_0, \mathbf{x}_m}$ is the material derivative along \mathbf{u}_0 taken at the position \mathbf{x}_m and expressed in the frequency domain. Additional variables in index refer to position or frequency for which the material derivative applies. After integrating over τ by recalling,

$$\int_{\mathbb{R}} d\tau e^{i(\omega + \omega_2)\tau} = 2\pi \delta(\omega + \omega_2) \quad (\text{B.13})$$

following formula is obtained for the acoustic spectral density S_{pp} ,

$$\begin{aligned} S_{pp}(\mathbf{x}_m, \omega) &= \frac{1}{2\pi} \int_{\Omega} d\mathbf{x}_1 \int_{\Omega} d\mathbf{x}_2 \int_{\mathbb{R}} d\tilde{t}_1 \int_{\mathbb{R}} d\tilde{t}_2 \int_{\mathbb{R}} d\omega_1 \int_{\mathbb{R}} d\omega_2 D_{-\mathbf{u}_0, \mathbf{x}_m} \left(\phi_{\mathbf{x}_m}^\dagger(\mathbf{x}_1, \omega_1) \right) \\ &\quad D_{-\mathbf{u}_0, \mathbf{x}_m} \left(\phi_{\mathbf{x}_m}^\dagger(\mathbf{x}_2, \omega_2) \right) e^{-i\omega_1 \tilde{t}_1 - i\omega_2 \tilde{t}_2} R_{QQ}(\mathbf{x}_1, \mathbf{x}_2, \tilde{t}_1 - \tilde{t}_2) \delta(\omega + \omega_2) \end{aligned} \quad (\text{B.14})$$

The straightforward evaluation of the integral over ω_2 along with the change of variable $\tilde{t}_2 = \tilde{t}_1 - \tilde{\tau}$ are performed,

$$\begin{aligned} S_{pp}(\mathbf{x}_m, \omega) &= \int_{\Omega} d\mathbf{x}_1 \int_{\Omega} d\mathbf{x}_2 \int_{\mathbb{R}} d\tilde{t}_1 \int_{\mathbb{R}} d\tilde{\tau} \int_{\mathbb{R}} d\omega_1 D_{-\mathbf{u}_0, \mathbf{x}_m} \left(\phi_{\mathbf{x}_m}^\dagger(\mathbf{x}_1, \omega_1) \right) \\ &\quad D_{-\mathbf{u}_0, \mathbf{x}_m} \left(\phi_{\mathbf{x}_m}^\dagger(\mathbf{x}_2, -\omega) \right) \frac{e^{-i\tilde{t}_1(\omega_1 - \omega)}}{2\pi} e^{-i\omega \tilde{\tau}} R_{QQ}(\mathbf{x}_1, \mathbf{x}_2, \tilde{\tau}) \end{aligned} \quad (\text{B.15})$$

which leads to equation (14) by the successive integrations over \tilde{t}_1 and ω_1 .

Appendix B.2. Fraunhofer's approximation

Fraunhofer's approximation considered here,

$$\phi_{\mathbf{x}_m}^\dagger(\mathbf{r} + \mathbf{x}_2, \omega) \approx \phi_{\mathbf{x}_m}^\dagger(\mathbf{x}_2, \omega) \exp\left(\frac{i\omega \mathbf{x}_m \cdot \mathbf{r}}{a_\infty |\mathbf{x}_m|}\right) \quad (\text{B.16})$$

differs from the one found in the literature [63],[51, eq. 14] by the sign of the phase-shift. This is due to the differences in reciprocity principle used by Tam and Auriault [62, eq. (2)] and by the authors [59, eq. (B5)]. Details on this formula are given in what follows. Only the difference in travel time between rays is accounted for, so that the ray coming from \mathbf{x}_2 is the same as the one from $\mathbf{x}_2 + \mathbf{r}$ but with an additional phase $\varphi = \mathbf{k} \cdot \mathbf{r}$, i.e. for the direct problem $\phi_{\mathbf{x}_2}^{(\mathbf{x}_m, \omega)} = \phi_{\mathbf{x}_2 + \mathbf{r}}^{(\mathbf{x}_m, \omega)} e^{i\varphi}$, where \mathbf{k} is the wave number pointing toward the observer point \mathbf{x}_m . Then for a medium at rest, $\varphi = \mathbf{k} \cdot \mathbf{r} = \frac{\omega}{a_\infty} \frac{(\mathbf{x}_m - \mathbf{x}_2)}{|\mathbf{x}_m - \mathbf{x}_2|} \cdot \mathbf{r} \approx \frac{\omega}{a_\infty} \frac{\mathbf{x}_m}{|\mathbf{x}_m|} \cdot \mathbf{r}$, so that, $\phi_{\mathbf{x}_2 + \mathbf{r}}^{(\mathbf{x}_m, \omega)} = \phi_{\mathbf{x}_2}^{(\mathbf{x}_m, \omega)} \exp\left(-i \frac{\omega}{a_\infty} \frac{\mathbf{x}_m}{|\mathbf{x}_m|} \cdot \mathbf{r}\right)$, the use of the reciprocity principle $\phi_{\mathbf{x}_s}^{(\mathbf{x}_m, \omega)} = \phi_{\mathbf{x}_m}^{(\mathbf{x}_s, \omega)^*}$ then provides equation (B.16). It is now shown how equation (16) is derived considering Fraunhofer's approximation. The quantity appearing in the integrand expresses then as,

$$\begin{aligned} D_{-\mathbf{u}_0, \mathbf{x}_m} \left(\phi_{\mathbf{x}_m}^\dagger(\mathbf{x}_2 + \mathbf{r}, \omega) \right) &= D_{-\mathbf{u}_0, \mathbf{x}_m} \left(\phi_{\mathbf{x}_m}^\dagger(\mathbf{x}_2, \omega) \right) \exp\left(\frac{i\omega \mathbf{x}_m \cdot \mathbf{r}}{a_\infty |\mathbf{x}_m|}\right) \\ &\quad - \phi_{\mathbf{x}_m}^\dagger(\mathbf{x}_2, \omega) \mathbf{u}_0 \cdot \frac{\partial}{\partial \mathbf{x}_m} \left(\exp\left(\frac{i\omega \mathbf{x}_m \cdot \mathbf{r}}{a_\infty |\mathbf{x}_m|}\right) \right) \end{aligned} \quad (\text{B.17})$$

Since $\frac{\partial}{\partial \mathbf{x}_m} \left(\frac{\mathbf{x}_m \cdot \mathbf{r}}{|\mathbf{x}_m|} \right) = \frac{|\mathbf{x}_m|^2 \mathbf{r} - (\mathbf{r} \cdot \mathbf{x}_m) \mathbf{x}_m}{|\mathbf{x}_m|^3}$, the derivative along \mathbf{u}_0 expresses as,

$$\begin{aligned} \mathbf{u}_0 \cdot \frac{\partial}{\partial \mathbf{x}_m} \left(\exp\left(\frac{i\omega \mathbf{x}_m \cdot \mathbf{r}}{a_\infty |\mathbf{x}_m|}\right) \right) &= i\omega \frac{|\mathbf{x}_m|^2 (\mathbf{u}_0 \cdot \mathbf{r}) - (\mathbf{r} \cdot \mathbf{x}_m) (\mathbf{u}_0 \cdot \mathbf{x}_m)}{a_\infty |\mathbf{x}_m|^3} \\ &\quad \exp\left(\frac{i\omega \mathbf{x}_m \cdot \mathbf{r}}{a_\infty |\mathbf{x}_m|}\right) \\ &\approx O\left(\frac{|\mathbf{r}|}{|\mathbf{x}_m|}\right) \end{aligned} \quad (\text{B.18})$$

550 where $|\mathbf{r}|/|\mathbf{x}_m|$ tends toward zero in Fraunhofer's approximation. Replacing this expression in the formula for S_{pp} , and by property of the Fourier transform

of real valued signals, $D_{-\mathbf{u}_0, \mathbf{x}_m} \left(\phi_{\mathbf{x}_m}^\dagger(\mathbf{x}_2, -\omega) \right) = \left[D_{-\mathbf{u}_0, \mathbf{x}_m} \left(\phi_{\mathbf{x}_m}^\dagger(\mathbf{x}_2, \omega) \right) \right]^*$, one obtains equation (16). From here on $\mathbf{x}_2 \equiv \mathbf{x}_s$, and two points in the source region are defined by the position and the separation vectors, \mathbf{x}_s and \mathbf{r} .

555 *Appendix B.3. Modelling of the source correlation term R_{QQ}*

Reproducing Tam and Auriault's change of variable for the integration, let $s = \tilde{\tau} - \mathbf{r} \cdot \mathbf{u}_0 / u_0^2$, then it comes $\mathbf{r} - \tilde{\tau} \mathbf{u}_0 = \mathbf{r}_\perp - s \mathbf{u}_0$, where $\mathbf{r}_\perp = \mathbf{r} - (\mathbf{r} \cdot \mathbf{u}_0) \mathbf{u}_0 / u_0^2$ is the projection of \mathbf{r} on the hyperplane associated to \mathbf{u}_0 so that $\mathbf{r}_\perp \cdot \mathbf{u}_0 = 0$. The source correlation term given in equation (17) then becomes,

$$R_{QQ}(\mathbf{x}_s, \mathbf{r}, \tilde{\tau}) = \frac{\hat{q}_s^2}{\tau_s^2} \exp \left(-\frac{|\mathbf{r} \cdot \mathbf{u}_0|}{u_0^2 \tau_s} - \frac{\ln(2)|\mathbf{r}_\perp|^2}{l_s^2} - \frac{\ln(2)u_0^2 s^2}{l_s^2} \right) \quad (\text{B.19})$$

After implementing this change of variable in the noise spectrum formula, one obtains,

$$S_{pp}(\mathbf{x}_m, \omega) = \int_{\Omega} d\mathbf{x}_s \frac{\hat{q}_s^2}{\tau_s^2} \left| D_{-\mathbf{u}_0, \mathbf{x}_m} \left(\phi_{\mathbf{x}_m}^\dagger(\mathbf{x}_s, \omega) \right) \right|^2 \left[\int_{\mathbb{R}} ds \exp \left(-\frac{\ln(2)u_0^2 s^2}{l_s^2} - i\omega s \right) \right] \underbrace{\left[\int_{\Omega} d\mathbf{r} \exp \left(-\frac{|\mathbf{r} \cdot \mathbf{u}_0|}{u_0^2 \tau_s} - \frac{\ln(2)|\mathbf{r}_\perp|^2}{l_s^2} + i\omega \mathbf{r} \cdot \left(\frac{\mathbf{x}_m}{a_\infty |\mathbf{x}_m|} - \frac{\mathbf{u}_0}{u_0^2} \right) \right) \right]}_{\mathcal{I}_r} \quad (\text{B.20})$$

The integration over ds can now be performed making use of [35, eq. (3.323), p.337 in 7th ed.] reprinted in § Appendix A.4,

$$\int_{\mathbb{R}} ds \exp \left(-\frac{\ln(2)u_0^2 s^2}{l_s^2} - i\omega s \right) = \frac{l_s}{u_0} \sqrt{\frac{\pi}{\ln(2)}} \exp \left(\frac{-\omega^2 l_s^2}{4 \ln(2) u_0^2} \right) \quad (\text{B.21})$$

The integration over \mathbf{r} can be performed using the split $\mathbf{r} = \mathbf{r}_\perp + \mathbf{r}_\parallel$ defined by the mean flow direction \mathbf{u}_0 , where $\mathbf{r}_\perp \cdot \mathbf{u}_0 = 0$ and $\mathbf{r}_\parallel \times \mathbf{u}_0 = \mathbf{0}$. The volume integral \mathcal{I}_r over \mathbf{r} can then be split into,

$$\mathcal{I}_r = \left[\int_{\mathbb{R}} d\mathbf{r}_\parallel \exp \left(-\frac{|\mathbf{r}_\parallel \cdot \mathbf{u}_0|}{u_0^2 \tau_s} + i\omega \mathbf{r}_\parallel \cdot \left(\frac{\mathbf{x}_m}{a_\infty |\mathbf{x}_m|} - \frac{\mathbf{u}_0}{u_0^2} \right) \right) \right] \left[\int_{\mathbb{R}^2} d\mathbf{r}_\perp \exp \left(-\frac{\ln(2)|\mathbf{r}_\perp|^2}{l_s^2} + \frac{i\omega \mathbf{r}_\perp \cdot \mathbf{x}_m}{a_\infty |\mathbf{x}_m|} \right) \right] \quad (\text{B.22})$$

The integral over $\mathbf{r}_{//}$ is evaluated using classical integral formula, given in § Appendix A.4, with $\mu = \frac{1}{u_0 \tau_s}$ and $\nu = \pm \frac{\omega}{u_0} \left(1 - \frac{\mathbf{u}_0 \cdot \mathbf{x}_m}{a_\infty |\mathbf{x}_m|}\right)$,

$$\int_{\mathbb{R}} d\mathbf{r}_{//} \exp\left(-\frac{|\mathbf{r}_{//} \cdot \mathbf{u}_0|}{u_0^2 \tau_s} + \frac{i\omega(\mathbf{r}_{//} \cdot \mathbf{u}_0)}{u_0^2} \left(\frac{\mathbf{u}_0 \cdot \mathbf{x}_m}{a_\infty |\mathbf{x}_m|} - 1\right)\right) = \frac{2u_0 \tau_s}{1 + \omega^2 \tau_s^2 \left(1 - \frac{\mathbf{u}_0 \cdot \mathbf{x}_m}{a_\infty |\mathbf{x}_m|}\right)^2} \quad (\text{B.23})$$

Similarly, the one running over \mathbf{r}_\perp is obtained with formula [35, eq. (3.323), p.337 in 7th ed.] reprinted in § Appendix A.4, setting $p_i = \frac{\sqrt{\ln(2)}}{l_s}$ and $q_i = \frac{i\omega x_i}{a_\infty |\mathbf{x}_m|}$ leading to,

$$\int_{\mathbb{R}^2} d\mathbf{r}_\perp \exp\left(-\frac{\ln(2)|\mathbf{r}_\perp|^2}{l_s^2} + \frac{i\omega \mathbf{r}_\perp \cdot \mathbf{x}_m}{a_\infty |\mathbf{x}_m|}\right) = \frac{\pi l_s^2}{\ln(2)} \exp\left(\frac{-\omega^2 l_s^2 |\mathbf{x}_{m,\perp}|^2}{4 \ln(2) a_\infty^2 |\mathbf{x}_m|^2}\right) \quad (\text{B.24})$$

where $\mathbf{x}_{m,\perp} = \mathbf{x}_m - (\mathbf{x}_m \cdot \mathbf{u}_0) \mathbf{u}_0 / u_0^2$. The double volume integral finally simplifies for this sound source model under Fraunhofer's condition into,

$$S_{pp}(\mathbf{x}_m, \omega) = \int_{\Omega} d\mathbf{x}_s \frac{2\hat{q}_s^2 l_s^3}{\tau_s} \left(\frac{\pi}{\ln(2)}\right)^{3/2} \left|D_{-\mathbf{u}_0, \mathbf{x}_m} \left(\phi_{\mathbf{x}_m}^\dagger(\mathbf{x}_2, \omega)\right)\right|^2 \frac{\exp\left(\frac{-\omega^2 l_s^2}{4 \ln(2) u_0^2} \left(1 + \frac{u_0^2 |\mathbf{x}_{m,\perp}|^2}{a_\infty^2 |\mathbf{x}_m|^2}\right)\right)}{1 + \omega^2 \tau_s^2 \left(1 - \frac{\mathbf{u}_0 \cdot \mathbf{x}_m}{a_\infty |\mathbf{x}_m|}\right)^2} \quad (\text{B.25})$$

Note additionally that the above expression differs from the original one by a factor of 2π , which is related to a different definition of Green's function, refer to [63, eq. (19)], from which a $4\pi^2$ factor appears; then because of differences in the Fourier transform conventions, see [63, eq. (25)], the present relation should be divided by 2π to comply with Tam and Auriault's relation.

Appendix B.4. Computation of $D_{-\mathbf{u}_0, \mathbf{x}_m} \left(\phi_{\mathbf{x}_m}^\dagger(\mathbf{x}_2, \omega)\right)$

In the previous expression the material derivative with reversed flow $D_{-\mathbf{u}_0, \mathbf{x}_m}$ of $\phi_{\mathbf{x}_m}^\dagger$ needs to be evaluated. When the observer is set in a region where the fluid is at rest, the derivation is straightforward. In other cases, the knowledge of the gradient of $\phi_{\mathbf{x}_m}^\dagger$ is required along the exterior mean flow \mathbf{u}_f . However

with the adjoint approach, Green's functions are solely known at the position \mathbf{x}_m . From a general point of view, the calculation of an estimate of $\mathbf{u}_0 \cdot \nabla \phi_{\mathbf{x}_m}^\dagger$ is possible by additionally computing the adjoint Green function $\phi_{\widetilde{\mathbf{x}}_m}^\dagger$, where $\widetilde{\mathbf{x}}_m = \mathbf{x}_m + \varepsilon \frac{\mathbf{u}_f}{|\mathbf{u}_f|}$ and $\varepsilon > 0$. An estimate for the material derivative follows,

$$\begin{aligned} D_{-\mathbf{u}_0, \mathbf{x}_m} \left(\phi_{\mathbf{x}_m}^\dagger(\mathbf{x}_s, \omega) \right) &= -i\omega \phi_{\mathbf{x}_m}^\dagger(\mathbf{x}_s, \omega) - \mathbf{u}_0 \cdot \nabla \phi_{\mathbf{x}_m}^\dagger(\mathbf{x}_s, \omega) \\ &= -i\omega \phi_{\mathbf{x}_m}^\dagger(\mathbf{x}_s, \omega) - |\mathbf{u}_f| \left(\frac{\phi_{\widetilde{\mathbf{x}}_m}^\dagger(\mathbf{x}_s, \omega) - \phi_{\mathbf{x}_m}^\dagger(\mathbf{x}_s, \omega)}{\varepsilon} \right)_{\varepsilon \rightarrow 0} \end{aligned} \quad (\text{B.26})$$

If the observer is set in the acoustic far-field this calculation can be done analytically even in presence of an ambient flow. Indeed $\phi_{\widetilde{\mathbf{x}}_m}^\dagger(\mathbf{x}_s, \omega)$ then differs from $\phi_{\mathbf{x}_m}^\dagger(\mathbf{x}_s, \omega)$ by only a phase shift φ , this is illustrated in the sketch given in figure B.15. The anti-causal adjoint field travels with a phase velocity

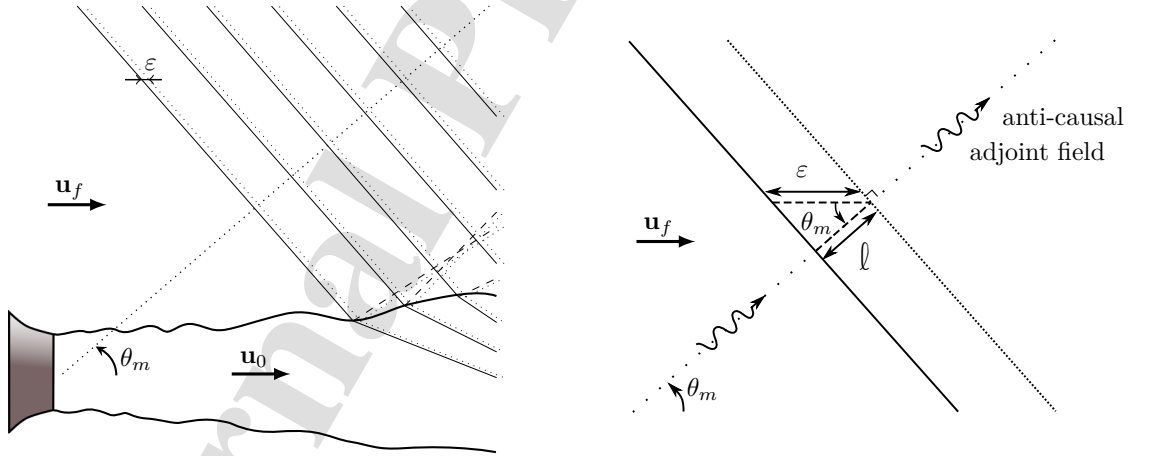


Figure B.15: Moving from ε the adjoint source in the acoustic far-field is equivalent to add a phase shift φ .

$|\mathbf{v}_p| = a_\infty + |\mathbf{u}_f| \cos \theta_m$ towards the observer set in the far-field. From the anti-causality property it comes $\phi_{\widetilde{\mathbf{x}}_m}^\dagger(\mathbf{x}_s, \omega) / \phi_{\mathbf{x}_m}^\dagger(\mathbf{x}_s, \omega) = e^{i\omega\varphi}$ with $\varphi > 0$. And

the previous expression is recast into,

$$D_{-\mathbf{u}_0, \mathbf{x}_m} \left(\phi_{\mathbf{x}_m}^\dagger(\mathbf{x}_s, \omega) \right) = \left(-i\omega - |\mathbf{u}_f| \left[\frac{e^{i\omega\varphi} - 1}{\varepsilon} \right]_{\varepsilon \rightarrow 0} \right) \phi_{\mathbf{x}_m}^\dagger(\mathbf{x}_s, \omega) \quad (\text{B.27})$$

The computation of φ with help of figure B.15 follows straightly, $\cos \theta_m = \ell/\varepsilon$ with $\ell = \varphi|\mathbf{v}_p|$. A Taylor expansion for small ε of the exponential function then readily gives,

$$D_{-\mathbf{u}_0, \mathbf{x}_m} \left(\phi_{\mathbf{x}_m}^\dagger(\mathbf{x}_s, \omega) \right) = \left(-i\omega - i \frac{\omega|\mathbf{u}_f| \cos \theta_m}{a_\infty + |\mathbf{u}_f| \cos \theta_m} \right) \phi_{\mathbf{x}_m}^\dagger(\mathbf{x}_s, \omega) \quad (\text{B.28})$$

Since the previous expression depends on the adjoint source location only by its polar angle θ_m , by defining $\phi_{\mathbf{x}_m}^\dagger(\mathbf{x}_s, \omega) \rightarrow \phi_{\theta_m}^\dagger(\mathbf{x}_s, \omega)$, a far-field expression for Tam and Auriault's mixing noise formula is obtained,

$$S_{pp}(\theta_m, \omega) = \int_{\Omega} d\mathbf{x}_s \frac{2\omega^2 \hat{q}_s^2 \tau_s^3}{\tau_s} \left(\frac{\pi}{\ln(2)} \right)^{3/2} \left| \phi_{\theta_m}^\dagger(\mathbf{x}_s, \omega) \right|^2 \left(1 + \frac{M_f \cos \theta_m}{1 + M_f \cos \theta_m} \right)^2 \frac{\exp \left(\frac{-\omega^2 \tau_s^2}{4 \ln(2) u_0^2} (1 + M_\infty^2 \sin^2 \theta_m) \right)}{1 + \omega^2 \tau_s^2 (1 - M_\infty \cos \theta_m)^2} \quad (\text{B.29})$$

where $M_\infty = u_0/a_\infty$ and $M_f = |\mathbf{u}_f|/a_\infty$. It is fairly straightforward to include in these derivations an azimuthal dependency on the microphone position ψ_m as well.

565 Appendix C. Free field analytical solution to Pierce's equation

In section § 2.2.3 and § 2.2.5, the squared absolute value of adjoint Green's function solution of Pierce's equation $|\phi_{\mathbf{x}_m}^\dagger|^2$ and the squared absolute value of its material derivative $|D_{-\mathbf{u}_0, \mathbf{x}_m}(\phi_{\mathbf{x}_m}^\dagger)|^2$ are involved in the computation of the acoustic spectral density S_{pp} . Free field adjoint Green's function for a medium with an uniform flow are derived here to the sake of validation. In a first approximation, only the movement of the surrounding medium is considered to model the acoustic propagation, and Pierce's equation reduces to the convected wave equation,

$$(-i\omega + \mathbf{u}_0 \cdot \nabla)^2 \phi_{\mathbf{x}_m}^\dagger - a_0^2 \Delta \phi_{\mathbf{x}_m}^\dagger = \delta_{\mathbf{x}_m} \quad (\text{C.1})$$

where $\delta_{\mathbf{x}_m}$ is an impulsive source set at the observer position. The boundary conditions of the adjoint problem are such as the solution is anti-causal, and the adjoint solution to the free field propagation problem expresses as [59],

$$\phi_{\mathbf{x}_m}^\dagger(\mathbf{x}) = \exp\left(-i \frac{\omega}{a_0} \frac{\mathbf{M}_0 \cdot (\mathbf{x} - \mathbf{x}_m)}{1 - M_0^2}\right) \frac{\exp\left(-i \frac{\omega}{a_0} \frac{r_{\mathbf{x}_m}}{1 - M_0^2}\right)}{4\pi a_0^2 r_{\mathbf{x}_m}} \quad (\text{C.2})$$

where $r_{\mathbf{x}_m} = \sqrt{(1 - M_0^2)|\mathbf{x} - \mathbf{x}_m|^2 + (\mathbf{M}_0 \cdot (\mathbf{x} - \mathbf{x}_m))^2}$, and $\mathbf{M}_0 = \mathbf{u}_0/a_0$ is the vectorial Mach number. It is worth remembering that this solution is such as the reciprocity principle is fulfilled,

$$\phi_{\mathbf{x}_m}^\dagger(\mathbf{x}) = \phi_{\mathbf{x}}(\mathbf{x}_m)^* \quad (\text{C.3})$$

Then by choosing the axis in such a way that the flow is oriented along the first direction, the material derivative $D_{-\mathbf{u}_0, \mathbf{x}_m}(\phi_{\mathbf{x}_m}^\dagger)$, expresses as,

$$D_{-\mathbf{u}_0, \mathbf{x}_m}(\phi_{\mathbf{x}_m}^\dagger(\mathbf{x})) = -i\omega\phi_{\mathbf{x}_m}^\dagger(\mathbf{x}) - u_{0,1} \frac{\partial \phi_{\mathbf{x}_m}^\dagger(\mathbf{x})}{\partial x_1} = \left(-i\omega + i\omega \frac{M_0}{1 - M_0^2} \left(M_0 + \frac{\partial r_{\mathbf{x}_m}}{\partial x_1}\right) + \frac{u_{0,1}}{r_{\mathbf{x}_m}} \frac{\partial r_{\mathbf{x}_m}}{\partial x_1}\right) \phi_{\mathbf{x}_m}^\dagger(\mathbf{x}) \quad (\text{C.4})$$

where $\partial r_{\mathbf{x}_m}/\partial x_1 = (x_1 - x_{m,1})/r_{\mathbf{x}_m}$, $\mathbf{x} = (x_1, x_2, x_3)^T$, $\mathbf{x}_m = (x_{m,1}, x_{m,2}, x_{m,3})^T$ and $\mathbf{u}_0 = (u_{0,1}, u_{0,2}, u_{0,3})^T$. A $(2\pi)^2$ difference with respect to the analytical solution derived in [47, eq. (49)-(50)] is noted. Remark other analytically known adjoint Green's function with a wider range of applicability could be considered [25, 62].

Appendix D. Adjoint maps at $\theta_m = 30^\circ$ and $\theta_m = 150^\circ$

Maps of adjoint Green's functions for Strouhal numbers $St = 0.3$ and $St = 0.9$ have been reported in § 4 for an observer located perpendicular to the jet axis in the acoustic far field. Corresponding cartography are displayed here for upstream and downstream observer positions forming shallow angles with respect to the jet axis. Adjoint Green's functions are shown for an observer at $\theta_m = 30^\circ$ in figures D.16 and D.17 and for an observer located at $\theta_m = 150^\circ$ in

figures D.18 and D.19. Results corresponding to Strouhal numbers $St= 0.3$ and $St= 0.9$ are presented respectively.

580 Compared to the computations performed at $\theta_m = 90^\circ$ and shown in figures 7 and 8, the presence of the jet flow causes stronger variations in the adjoint fields computed for these shallow observer angles. The fields obtained for upstream and downstream observers are however substantially different. At $\theta_m = 30^\circ$ the jet flow causes a significant reflection of the adjoint field in the form of a
585 horseshoe, creating a shielding in the area masked by the jet. This is most easily seen in the absolute value of adjoint Green's function presented in figure D.17. The acoustic reflection observed at this angle lead to low amplitudes of adjoint Green's functions in the jet potential core. At $\theta_m = 150^\circ$ the shielding does not happen, and the levels of the adjoint fields in the region masked by the jet
590 flow are comparable with the area directly visible from the observer location. Maximum amplitudes of adjoint Green's functions are found, this time, in the jet potential core and in the duct. As for adjoint fields calculated for an observer at $\theta_m = 90^\circ$, the adjoint fields present modal structures in the jet plume. Their amplitudes at $\theta_m = 150^\circ$ are however much higher.

595 The complete integrand of Tam and Auriault's mixing noise formula are presented for these two observer angles and two Strouhal numbers. At $\theta_m = 30^\circ$, the shear layer region directly visible from the observer location has the largest contribution. This area is the main one selected by the squared absolute value of adjoint Green's functions. At $\theta_m = 150^\circ$, modulation of the visible part as
600 well as modulation of the hidden part of the shear layer contribute to the sound pressure level computed. For this upstream located observer, the shear layer part masked by the jet flow is seen to contribute the most significantly.

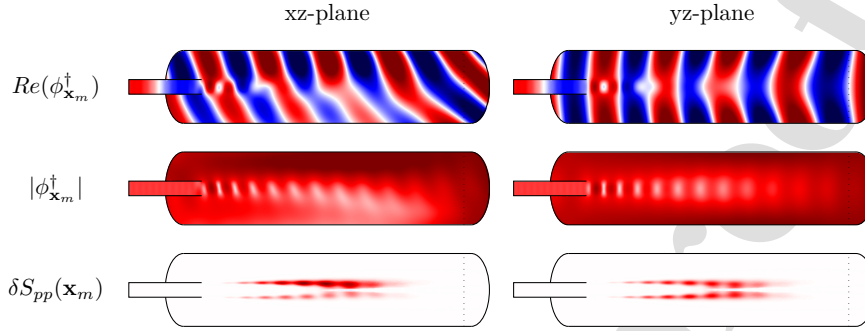


Figure D.16: Real part and absolute part of adjoint Green's function $\phi_{\mathbf{x}_m}^\dagger$ for an observer at $\theta_m = 30^\circ$ and $St = 0.3$. The resulting modulation of the integrand $\delta S_{pp}(\mathbf{x}_m)$ is depicted. $Re(\phi_{\mathbf{x}_m}^\dagger) \in [-3, 3] \times 10^{-6}$ Pa.s and $|\phi_{\mathbf{x}_m}^\dagger| \in [0, 4] \times 10^{-6}$ Pa.s.

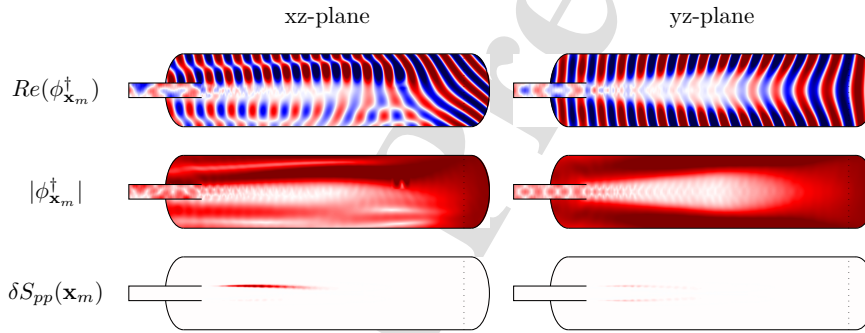


Figure D.17: Real part and absolute part of adjoint Green's function $\phi_{\mathbf{x}_m}^\dagger$ for an observer at $\theta_m = 30^\circ$ and $St = 0.9$. The resulting modulation of the integrand $\delta S_{pp}(\mathbf{x}_m)$ is depicted. $Re(\phi_{\mathbf{x}_m}^\dagger) \in [-3, 3] \times 10^{-6}$ Pa.s and $|\phi_{\mathbf{x}_m}^\dagger| \in [0, 4] \times 10^{-6}$ Pa.s.

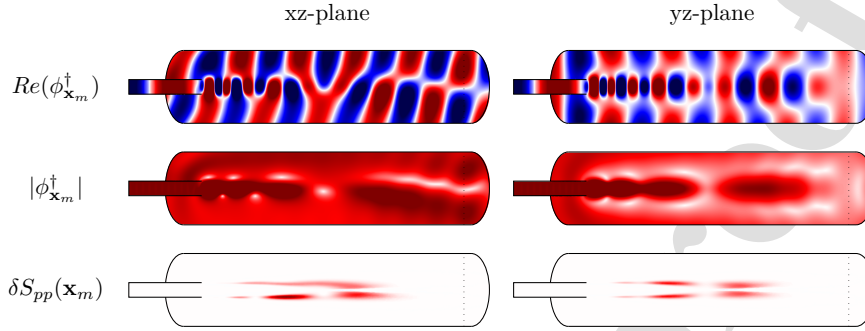


Figure D.18: Real part and absolute part of adjoint Green's function $\phi_{\mathbf{x}_m}^\dagger$ for an observer at $\theta_m = 150^\circ$ and $St = 0.3$. The resulting modulation of the integrand $\delta S_{pp}(\mathbf{x}_m)$ is depicted. $Re(\phi_{\mathbf{x}_m}^\dagger) \in [-3, 3] \times 10^{-6}$ Pa.s and $|\phi_{\mathbf{x}_m}^\dagger| \in [0, 4] \times 10^{-6}$ Pa.s.

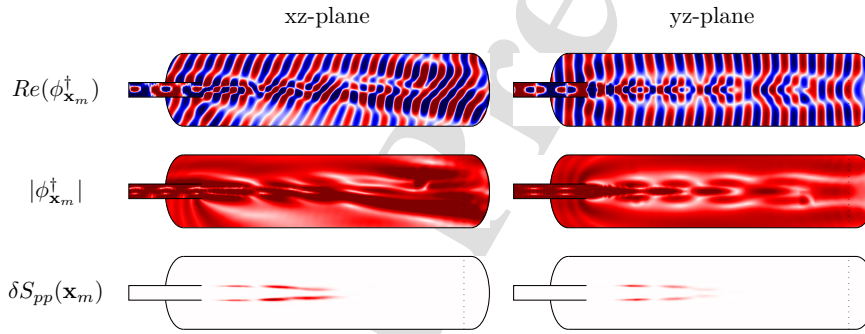


Figure D.19: Real part and absolute part of adjoint Green's function $\phi_{\mathbf{x}_m}^\dagger$ for an observer at $\theta_m = 150^\circ$ and $St = 0.9$. The resulting modulation of the integrand $\delta S_{pp}(\mathbf{x}_m)$ is depicted. $Re(\phi_{\mathbf{x}_m}^\dagger) \in [-3, 3] \times 10^{-6}$ Pa.s and $|\phi_{\mathbf{x}_m}^\dagger| \in [0, 4] \times 10^{-6}$ Pa.s.

Appendix E. Sensitivity analysis for adjoint Green's functions computed at $\theta_m = 150^\circ$

605 In § 5.1, a base flow representative of the jet averaged flow profile (a), a
simplified cylindrical vortex sheet model (c), along with a hybrid combination of
the two that includes the duct geometry and a downstream smoothed truncation
of the jet flow (c), have been considered. Configurations (a) and (c) model
the duct as semi-infinite by absorbing the acoustic energy that enters into it
610 by means of PML. The frequency of the tones predicted did not significantly

vary for these various cases. In § 5.2, the effect of the acoustic reflection in the duct has been investigated by considering a total reflection of the acoustic penetrating in the conduit. This last configuration, denoted (a-HW) in what follows, considers identical flow and pipe length as in case (a) but assumes a total reflection in the pipe. Compared to cases (a), (b) and (c), a tangible modification of the tone signature has been observed in this configuration. In all these cases the sound source model is unchanged, only adjoint Green's functions differ. This section compares visualisations in the xz -plane of the latter quantity to gain a broader understanding of the generation process of upstream travelling guided jet modes.

Absolute value of adjoint Green's functions for the cases studied in § 5 are shown in figure E.20 for Strouhal numbers $St=0.27$, that corresponds to the first tone, and $St=0.34$, that is associated with the minima between the first and second peak. The noise level in Tam and Auriault's model is obtained from the scalar product of the absolute value of adjoint Green's functions and the sound source model, thus only the region of adjoint Green's function for which the sound source is non-zero are meaningful. In these regions, for the first peak at $St=0.27$, adjoint fields computed for identical base flows are identical, i.e. the field in figure E.20 (a) resembles to that in figure E.20 (a - HW), and that in figure E.20 (b) resembles to that in figure E.20 (c). These similarities are retrieved in the acoustic predictions presented in figure 11 and in figure 12 (a). The acoustic energy in the duct is not directly correlated with the **in-duct** boundary condition, and the effect of nozzle impedance is not recognisable at the Strouhal number of the tone. At Strouhal number $St=0.34$, that is for the minima between the first and the second tone, a 3 dB difference in the noise spectra was observed between the case that model acoustic reflection in the duct (a-HW), and the configuration that does not (a). Comparing the structure of the adjoint fields of the second column in figure E.20, solutions for case (b) and case (c) are again alike in shape and amplitude. The case (a) and the case (a - HW) present similar structure of adjoint fields, but their amplitudes are significantly different and account for the additional 3 dB predicted.

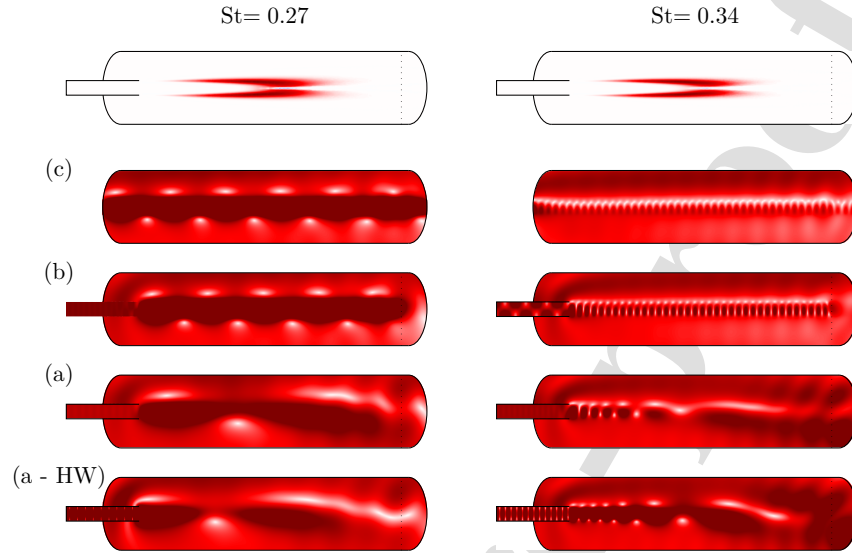


Figure E.20: Tam and Auriault's mixing noise source model, and corresponding adjoint Green's functions $|\phi_{\mathbf{x}_m}^\dagger|$ in the xz -plane for $St= 0.27$ and $St= 0.34$ computed for an observer set at $\theta_m = 150^\circ$. The modelled sound source is represented in the first row, it corresponds to the complete integrand of equation (18) leaving aside the material derivative of adjoint Green's function. The three central rows present the solution obtained for the configuration of figure 10, the last row shows the result obtained for a case identical to case (a) but with a permeable hard-wall boundary condition to model **in-duct** reflections. $|\phi_{\mathbf{x}_m}^\dagger| \in [0, 4] \times 10^{-6}$ Pa.s.

Structure of adjoint fields tailored to the four cases studied are presented in figure E.21 for Strouhal numbers corresponding to the second and the third tone computed, that is for $St= 0.52$ and $St= 0.82$. The global structure of adjoint
 645 Green's functions for cases assuming a flow model with infinitely thin shear layer differ noticeably from fields considering a realistic base flow. Regular patterns in the streamwise direction are visible for the adjoint fields that consider the plug flow model which are absent from the more realistic flow model. However, in the region where the sound source is significant, different tailored adjoint Green's
 650 functions are fairly comparable.

The azimuthal and radial structure of the modes in the jet for the Strouhal

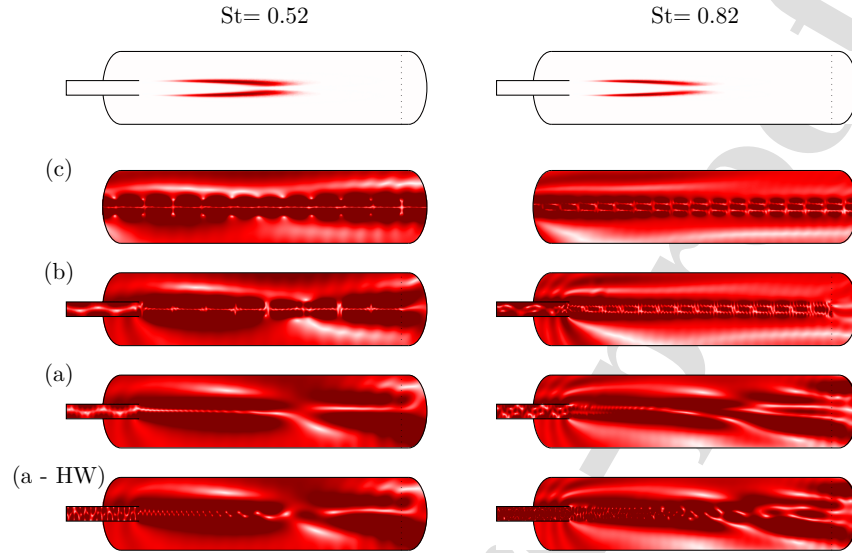


Figure E.21: Tam and Auriault's mixing noise source model, and corresponding adjoint Green's functions $|\phi_{\mathbf{x}_m}^\dagger|$ in the xz -plane for $St= 0.52$ and $St= 0.82$ computed for an observer set at $\theta_m = 150^\circ$. The modelled sound source is represented in the first row, it corresponds to the complete integrand of equation (18) leaving aside the material derivative of adjoint Green's function. The three central rows present the solution obtained for the configuration of figure 10, the last row shows the result obtained for a case identical to case (a) but with a permeable hard-wall boundary condition to model **in-duct** reflections. $|\phi_{\mathbf{x}_m}^\dagger| \in [0, 4] \times 10^{-6}$ Pa.s.

numbers of the first three tones are presented in figure E.22 for the case (a). Real part and absolute part of adjoint Green's functions extracted at $z/D_J = 5.0$ downstream of the duct are shown. The duct section is marked with a dotted
 655 circle. Tam and Ahuja [61] gave the (n_θ, n_r) eigenfunction distribution of the neutral wave modes, where n_θ corresponds to the azimuthal mode order and n_r is the radial order. Looking at the real part of the structure presented in figure E.22, a (0,1) mode is obtained for the first tone, a (1,1) mode for the second and a (2,1) mode for the third tone. Remarkably, the structure of these adjoint
 660 fields comply with the physical ones [14]. The contributing part of the jet can be deduced from the absolute value of adjoint Green's functions. At this axial

location, it appears for the third tone, that the major contribution of the shear layer originates from the area masked by the jet.

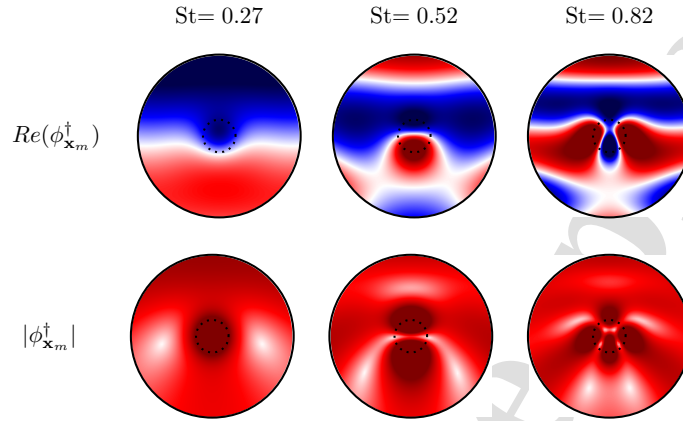


Figure E.22: Real part and absolute part of adjoint Green's function $\phi_{\mathbf{x}_m}^\dagger$ computed for the case (a) and an observer at $\theta_m = 150^\circ$. The Strouhal numbers corresponding to the first three tones are considered, extracts at $z/D_J = 5.0$ downstream of the duct exhaust are presented. $Re(\phi_{\mathbf{x}_m}^\dagger) \in [-3, 3] \times 10^{-6}$ Pa.s and $|\phi_{\mathbf{x}_m}^\dagger| \in [0, 4] \times 10^{-6}$ Pa.s.

References

- 665 [1] A. Adam, D. Papamoschou, and C. Bogey. Imprint of vortical structures on the near-field pressure of a turbulent jet. *AIAA J.*, 60(3), 2022.
- [2] M. Z. Afsar. Solution of the parallel shear layer Green's function using conservation equations. *Int. J. Aeroacoustics*, 8(6):585–602, 2009.
- [3] M. Z. Afsar. Asymptotic properties of the overall sound pressure level of
670 subsonic jet flows using isotropy as a paradigm. *J. Fluid Mech.*, 664:510–539, 2010.
- [4] M. Z. Afsar. Insight into the two-source structure of the jet noise spectrum using a generalized shell model of turbulence. *Eur. J. Mech. B Fluids*, 31:129–139, 2012.

- 675 [5] M. Z. Afsar, V. Gryazev, A. Markesteijn, and S. A. Karabasov. Effect of tensor representations for high-order turbulence correlations in complex axi-symmetric flow fields. In *AIAA Aviation 2021 Forum*, page 2280, Virtual event, 2021. AIAA Paper 2021-2280.
- [6] M. Z. Afsar, A. Sescu, V. Gryazev, A. P. Markesteijn, and S. A. Karabasov. 680 Analysis of the non-parallel flow-based Green's function in the acoustic analogy for complex axisymmetric jets. In *26th AIAA/CEAS Aeroacoustics Conference*, Virtual event, 2020. AIAA Paper 2020-2507.
- [7] M. Z. Afsar, A. Sescu, and S. J. Leib. Modelling and prediction of the peak-radiated sound in subsonic axisymmetric air jets using acoustic analogy-based asymptotic analysis. *Philos. Trans. Royal Soc. A*, 685 377(2159):20190073, 2019.
- [8] M. Z. Afsar, A. Sescu, and V. Sassanis. Effect of non-parallel mean flow on the acoustic spectrum of heated supersonic jets: Explanation of “jet quietening”. *Phys. Fluids*, 31(10):105107, 2019.
- 690 [9] C. Bailly, C. Bogey, and S. Candel. Modelling of Sound Generation by Turbulent Reacting Flows. *Int. J. Aeroacoustics*, 9(4-5):461–489, 2010.
- [10] C. Bailly and G. Comte-Bellot. *Turbulence*. Experimental Fluid Mechanics. Springer, Heidelberg, 2015.
- [11] C. Bailly, P. Lafon, and S. M. Candel. Subsonic and supersonic jet noise 695 predictions from statistical source models. *AIAA J.*, 35(11):1688–1696, 1997.
- [12] A. Bassetti and J. W. Nichols. Analysis of LES for source modeling in jet noise. In *20th AIAA/CEAS Aeroacoustics Conference*, Atlanta, Georgia, 2014. AIAA Paper 2014-2905.
- 700 [13] C. Bogey. Grid sensitivity of flow field and noise of high-Reynolds-number jets computed by large-eddy simulation. *Int. J. Aeroacoustics*, 17(4-5):399–424, 2018.

- [14] C. Bogey. Acoustic tones in the near-nozzle region of jets: characteristics and variations between Mach numbers 0.5 and 2. *J. Fluid Mech.*, 921:A3, 2021.
- 705
- [15] C. Bogey. Generation of excess noise by jets with highly disturbed laminar boundary-layer profiles. *AIAA J.*, 59(2):569–579, 2021.
- [16] C. Bogey. A database of flow and near pressure field signals obtained for subsonic and nearly ideally expanded supersonic free jets using large-eddy simulations. <https://hal.archives-ouvertes.fr/hal-03626787>, 2022.
- 710
- [17] C. Bogey. Tones in the acoustic far field of jets in the upstream direction. *AIAA J.*, 60(4), 2022.
- [18] C. Bogey and C. Bailly. An analysis of the correlations between the turbulent flow and the sound pressure fields of subsonic jets. *J. Fluid Mech.*, 583:71–97, 2007.
- 715
- [19] C. Bogey, C. Bailly, and D. Juvé. Computation of flow noise using source terms in linearized Euler’s equations. *AIAA J.*, 40(2):235–243, 2002.
- [20] C. Bogey, S. Barré, V. Fleury, C. Bailly, and D. Juvé. Experimental study of the spectral properties of near-field and far-field jet noise. *Int. J. Aeroacoustics*, 6(2):73–92, 2007.
- 720
- [21] C. Bogey, O. Marsden, and C. Bailly. Large-eddy simulation of the flow and acoustic fields of a Reynolds number 10^5 subsonic jet with tripped exit boundary layers. *Phys. Fluids*, 23(3):035104, 2011.
- [22] C. Bogey and R. Sabatini. Effects of nozzle-exit boundary-layer profile on the initial shear-layer instability, flow field and noise of subsonic jets. *J. Fluid Mech.*, 876:288–325, 2019.
- 725
- [23] A. V. G. Cavalieri, P. Jordan, W. R. Wolf, and Y. Gervais. Scattering of wavepackets by a flat plate in the vicinity of a turbulent jet. *J. Sound Vib.*, 333(24):6516–6531, 2014.

- 730 [24] N. K. Depuru Mohan, A. P. Dowling, S. A. Karabasov, H. Xia, O. Graham,
T. P. Hynes, and P. G. Tucker. Acoustic sources and far-field noise of
chevron and round jets. *AIAA J.*, 53(9):2421–2436, 2015.
- [25] A. P. Dowling, J. E. Ffowcs Williams, and M. E. Goldstein. Sound produc-
tion in a moving stream. *Philos. Trans. Royal Soc. A*, 288(1353):321–349,
735 1978.
- [26] ECAC. Doc 29, 4th ed. “Report on standard method of computing noise
contours around civil airports”, volume 1: Applications guide. Technical
report, DGCA/147, 2016.
- [27] T. Emmert, P. Lafon, and C. Bailly. Numerical study of self-induced tran-
sonic flow oscillations behind a sudden duct enlargement. *Phys. Fluids*,
740 21(10):106105, 2009.
- [28] V. Fleury, C. Bailly, E. Jondeau, M. Michard, and D. Juvé. Space-time
correlations in two subsonic jets using dual particle image velocimetry mea-
surements. *AIAA J.*, 46(10):2498–2509, 2008.
- 745 [29] M. E. Goldstein. A generalized acoustic analogy. *J. Fluid Mech.*, 488:315–
333, 2003.
- [30] M. E. Goldstein. Ninety-degree acoustic spectrum of a high speed air jet.
AIAA J., 43(1):96–102, 2005.
- [31] M. E. Goldstein and S. J. Leib. The aeroacoustics of slowly diverging
750 supersonic jets. *J. Fluid Mech.*, 600:291–337, 2008.
- [32] M. E. Goldstein and S. J. Leib. Azimuthal source noncompactness and
mode coupling in sound radiation from high-speed axisymmetric jets. *AIAA
J.*, 56(10):3915–3925, 2018.
- 755 [33] M. E. Goldstein and B. Rosenbaum. Effect of anisotropic turbulence on
aerodynamic noise. *J. Acoust. Soc. Am.*, 54(3):630–645, 1973.

- [34] M. E. Goldstein, A. Sescu, and M. Z. Afsar. Effect of non-parallel mean flow on the Green's function for predicting the low-frequency sound from turbulent air jets. *J. Fluid Mech.*, 695:199–234, 2012.
- [35] I. S. Gradshteyn and I. M. Ryzhik. *Table of Integrals, Series, and Products*. Academic Press, New York, 1965.
- [36] M. S. Howe. *Acoustics of fluid-structure interactions*. Cambridge university press, 1998.
- [37] U. Ingard and V. K. Singhal. Effect of flow on the acoustic resonances of an open-ended duct. *J. Acoust. Soc. Am.*, 58(4):788–793, 1975.
- [38] S. A. Karabasov and T. P. Hynes. Adjoint linearised Euler solver in the frequency domain for jet noise modelling. In *12th AIAA/CEAS Aeroacoustics Conference*, Cambridge, Massachusetts, 2006. AIAA Paper 2006-2673.
- [39] A. Z. Karon and K. K. Ahuja. Role of nozzle-exit boundary layer in producing jet noise. *Int. J. Aeroacoustics*, 0(1-28), 2022.
- [40] A. Khavaran and J. Bridges. Modelling of fine-scale turbulence mixing noise. *J. Sound Vib.*, 279(3-5):1131–1154, 2005.
- [41] J. L. Lagrange. Nouvelles recherches sur la nature et la propagation du son. *Oeuvres*, 1:151–332, 1761.
- [42] S. J. Leib and M. E. Goldstein. Hybrid source model for predicting high-speed jet noise. *AIAA J.*, 49(7):1324–1335, 2011.
- [43] S. J. Leib, D. Ingraham, and J. E. Bridges. Evaluating source terms of the generalized acoustic analogy using the jet engine noise reduction (JENRE) code. In *55th AIAA Aerospace Sciences Meeting*, Grapevine, Texas, 2017. AIAA Paper 2017-0459.
- [44] M. J. Lighthill. On sound generated aerodynamically I. General theory. In *Proc. R. Soc. Lond. A*, volume 1107, pages 564–587. The Royal Society London, 1952.

- [45] G. M. Lilley, H. E. Plumblee, W. C. Strahle, S. Y. Ruo, and P. E. Doak. The generation and radiation of supersonic jet noise. Volume IV. Theory of turbulence generated jet noise, noise radiation from upstream sources, and combustion noise. Technical report, Lockheed-Georgia Co. Marietta, 1972.
- [46] W. Möhring. A well posed acoustic analogy based on a moving acoustic medium. In *Aeroacoustic workshop SWING*, Dresden, 1999.
- [47] P. J. Morris and F. Farassat. Acoustic analogy and alternative theories for jet noise prediction. *AIAA J.*, 40(4):671–680, 2002.
- [48] S. Piantanida, V. Jaunet, J. Huber, W. R. Wolf, P. Jordan, and A. V. G. Cavalieri. Scattering of turbulent-jet wavepackets by a swept trailing edge. *J. Acoust. Soc. Am.*, 140(6):4350–4359, 2016.
- [49] A. D. Pierce. Wave equation for sound in fluids with unsteady inhomogeneous flow. *J. Acoust. Soc. Am.*, 87(6):2292–2299, 1990.
- [50] P. Pineau and C. Bogey. Numerical investigation of wave steepening and shock coalescence near a cold mach 3 jet. *J. Acoust. Soc. Am.*, 149(1):357–370, 2021.
- [51] N. Raizada and P. J. Morris. Prediction of noise from high speed subsonic jets using an acoustic analogy. In *12th AIAA/CEAS Aeroacoustics Conference*, Cambridge, Massachusetts, 2006. AIAA Paper 2006-2596.
- [52] H. S. Ribner. Aerodynamic sound from fluid dilitations. A theory of the sound from jets and other flows. Technical report, University of Toronto, Institute of aerophysics, 1962. UTIA Report N° 86, AFOSR TN 3430.
- [53] H. S. Ribner. Quadrupole correlations governing the pattern of jet noise. *J. Fluid Mech.*, 38(1):1–24, 1969.
- [54] A. Ruggiero, R. D’Amato, and S. Affatato. Comparison of meshing strategies in THR finite element modelling. *Materials*, 12(14):2332, 2019.

- 810 [55] O. T. Schmidt, A. Towne, T. Colonius, A. V. G. Cavalieri, P. Jordan, and
G. A. Brès. Wavepackets and trapped acoustic modes in a turbulent jet:
coherent structure eduction and global stability. *J. Fluid Mech.*, 825:1153–
1181, 2017.
- [56] R. H. Self and M. Azarpeyvand. Utilization of turbulent energy transfer
815 rate time-scale in aeroacoustics with application to heated jets. *Int. J.*
Aeroacoustics, 7(2):83–102, 2008.
- [57] L. Selle, F. Nicoud, and T. Poinso. Actual impedance of nonreflecting
boundary conditions: Implications for computation of resonators. *AIAA*
J., 42(5):958–964, 2004.
- 820 [58] V. A. Semiletov and S. A. Karabasov. A 3D frequency-domain linearised
Euler solver based on the Goldstein acoustic analogy equations for the
study of nonuniform meanflow propagation effects. In *19th AIAA/CEAS*
Aeroacoustics Conference, Berlin, 2013. AIAA Paper 2013-2019.
- [59] É. Spieser and C. Bailly. Sound propagation using an adjoint-based method.
825 *J. Fluid Mech.*, 900:A5, 2020.
- [60] É. Spieser, C. Legendre, and C. Bailly. Solution of Pierce’s equation for
Tam & Auriault’s mixing noise model. In *AIAA Aviation 2021 Forum*,
page 2238, Virtual event, 2021. AIAA Paper 2021-2238.
- [61] C. K. W. Tam and K. K. Ahuja. Theoretical model of discrete tone gener-
830 ation by impinging jets. *J. Fluid Mech.*, 214:67–87, 1990.
- [62] C. K. W. Tam and L. Auriault. Mean flow refraction effects on sound
radiated from localized source in a jet. *J. Fluid Mech.*, 370:149–174, 1998.
- [63] C. K. W. Tam and L. Auriault. Jet mixing noise from fine-scale turbulence.
AIAA J., 37(2):145–153, 1999.
- 835 [64] C. K. W. Tam, M. Golebiowski, and J. Seiner. On the two components of
turbulent mixing noise from supersonic jets. In *2nd AIAA/CEAS Aeroa-*

- oustics Conference*, State College, Pennsylvania, 1996. AIAA Paper 1996-1716.
- [65] C. K. W. Tam, N. N. Pastouchenko, and K. Viswanathan. Continuation
840 of near-acoustic fields of jets to the far field. part I: Theory. In *16th AIAA/CEAS Aeroacoustics Conference*, Stockholm, 2010. AIAA Paper 2010-3728.
- [66] C. K. W. Tam, K. Viswanathan, N. N. Pastouchenko, and B. Tam. Contin-
845 uation of near-acoustic fields of jets to the far field. part II: Experimental validation and noise source characteristics. In *16th AIAA/CEAS Aeroacoustics Conference*, Stockholm, 2010. AIAA Paper 2010-3729.
- [67] A. Towne, G. A Brès, and S. K. Lele. A statistical jet-noise model based on the resolvent framework. In *23rd AIAA/CEAS Aeroacoustics Conference*, Denver, Colorado, 2017. AIAA Paper 2017-3706.
- 850 [68] A. Towne, A. V. G. Cavalieri, P. Jordan, T. Colonius, O. Schmidt, V. Jaunet, and G. A. Brès. Acoustic resonance in the potential core of subsonic jets. *J. Fluid Mech.*, 825:1113–1152, 2017.
- [69] B. Van Antwerpen, Y. Detandt, D. Copiello, E. Rosseel, and E. Gaudry. Performance improvements and new solution strategies of Actran TM for
855 nacelle simulations. In *20th AIAA/CEAS Aeroacoustics Conference*, Atlanta, Georgia, 2014. AIAA Paper 2014-2315.
- [70] K. B. M. Q. Zaman. Effect of initial boundary-layer state on subsonic jet noise. *AIAA J.*, 50(8):1784–1795, 2012.
- 860 [71] K. B. M. Q. Zaman, A. F. Fagan, and P. Upadhyay. Pressure fluctuations due to ‘trapped waves’ in the initial region of compressible jets. *J. Fluid Mech.*, 931, 2022.

- + Tam & Auriault's mixing noise model is recast to be calibration-free and robust
- + Adjoint method is used to identify the radiated part of sound sources in jets
- + Pierce's wave equation provides an energy preserving formulation to sound propagation
- + Tailored adjoint Green's function of Pierce's equation solved with Actran FEM solver
- + Tones of upstream propagating guided jet waves are predicted in this framework

Journal Pre-proof